Synthesis and Characterization of Single Phase $Zr_{0.5}Y_{0.5}B_{12}$

Georgiy Akopov[1,2,3], Wai H. Mak[1], Dimitrios Koumoulis[1], Hang Yin[1], Bryan Owens-Baird[2,3], Michael T. Yeung[4], Mit H. Muni[1], Shannon Lee[2], Inwhan Roh[1,5], Zachary C. Sobell[1,7], Gourab Bhaskar[2], Paula L. Diaconescu[1], Julia V. Zaikina[2], Reza Mohammadi[7], Kirill A. Kovnir[2,3*] and Richard B. Kaner[1,8,9*]*

[1]*Department of Chemistry and Biochemistry, University of California, Los Angeles (UCLA), Los Angeles, CA 90095, USA*

[2]*Department of Chemistry, Iowa State University, Ames, IA 50011, USA*

[3]*Ames Laboratory, U.S. Department of Energy, Ames, IA 50011, USA*

[4]*Department of Chemistry, Northwestern University, Evanston, IL 60208, USA*

[5]*College of Chemistry, University of California, Berkeley, Berkeley, CA 94720, USA*

[6]*Department of Chemistry and Biochemistry, University of Colorado Boulder, Boulder, CO 80309*

[7]*Department of Mechanical and Nuclear Engineering, Virginia Commonwealth University, Richmond, VA 23284, USA*

[8]*Department of Materials Science and Engineering, University of California, Los Angeles (UCLA), Los Angeles, CA 90095, USA*

[9]*California NanoSystems Institute (CNSI), University of California, Los Angeles (UCLA), Los Angeles, CA 90095, USA*

* Corresponding authors: rmohammadi@vcu.edu, kovnir@iasate.edu, kaner@chem.ucla.edu

ABSTRACT

The single-phase metal dodecaboride (MB_{12}) solid solutions $Zr_{0.5}Y_{0.5}B_{12}$ and $Zr_{0.5}U_{0.5}B_{12}$ were prepared by arc-melting. The phase purity and composition were established by powder X-ray diffraction (XRD), Energy-dispersive X-ray spectroscopy (EDS), X-ray photoelectron spectroscopy (XPS), and ^{10}B and ^{11}B solid state NMR spectroscopy. The effect of carbon addition to $Zr_{1-x}Y_xB_{12}$ was studied and it was found that carbon causes fast cooling and, as a result, rapid nucleation of grains, as well as "templating" and patterning effects of the surface morphology. The hardness of the $Zr_{0.5}Y_{0.5}B_{12}$ phase is 47.6 ± 1.7 GPa at 0.49 N load, which is ~17% higher than that of its parent compounds, ZrB_{12} and YB_{12}, with hardnesses of 41.6 ± 2.6 and 37.5 ± 4.3 GPa, respectively. The hardness of $Zr_{0.5}U_{0.5}B_{12}$ is ~54% higher than that of its UB_{12} parent. The dodecaborides were confirmed to be metallic by band structure calculations, diffuse reflectance UV-Visvis spectroscopy and NMR spectroscopy. The nature of the dodecaboride colors – violet for ZrB_{12} and blue for YB_{12} – can be attributed to charge transfer. XPS indicated that the metals are in the following oxidation states: Y^{+3}, Zr^{+4} and $U^{+5/+6}$. The superconducting transition temperatures (T_c) of the dodecaborides were determined to be ~5 - 6 K for both ZrB_{12} and YB_{12}, as shown by resistivity and SQUID (superconducting quantum interference device) measurements. The T_c of the solid solution was suppressed to ~3 – 3.5 K.

INTRODUCTION

The compositional breadth of metal borides has resulted in a remarkable range of crystal structures.[1,2] This structural diversity yields exciting optical, magnetic and electronic,[3–7] catalytic,[8,9] and mechanical properties.[1,10–12] Metal boride structures range from metal rich sub-borides[13] (M_4B) to mono-,[14,15] di-[16,17] and tetraborides,[18–20] to boron rich borides: dodecaborides[21] (MB_{12}) and higher borides[22] (MB_{66}), and β-rhombohedral boron doping phases[23,24] (MB_{50-100}); as well as ternary and higher metal borides.[1,25] Of the aforementioned boride families, metal dodecaborides are interesting due not only to having superior mechanical properties (superhardness),[26–29] but also interesting optical (color)[26–28] and electronic (superconductivity)[30] properties, as well as good oxidation resistance.[26]

Metal dodecaborides can crystallize in two different structures: *cubic*-UB_{12} ($Fm\bar{3}m$) and *tetragonal*-ScB_{12} (*I4/mmm*) (**Figure 1**).[1,21,26] The majority of metals form the cubic phase[1,21] and only Sc, as well as solid solutions of ScB_{12} with another metal (at <5 atom% secondary metal addition), crystallizes in the tetragonal structure.[26,31,32] The dodecaboride structure can be thought of as a face-centered cubic (FCC) or body-centered tetragonal (BCT) for ScB_{12} lattice of 12-coordinate metal atoms, each surrounded by a 24 boron atom cuboctahedron cage. Whether a metal can form a dodecaboride phase is primarily determined by the size of the metal in a 12 coordinate environment; generally, the metal has to have a 12-coordinate radius in between that of zirconium (1.603 Å) and yttrium (1.801 Å).[28,33] Moreover, slight deviations from this range, as in the case of hafnium (1.580 Å)[34] and gadolinium, require high-pressure (6.5 GPa) synthesis[33,34] or ambient pressure stabilization via solid-solution formation ($Y_{1-x}Hf_xB_{12}$ and $Zr_{1-x}Gd_xB_{12}$).[27–29]

Most metal dodecaboride phases are incongruently melting, and as such can either be formed as MB_{12} and a lower boride (e.g. ZrB_2 and YB_6) or as MB_{12} and a higher boride or crystalline boron (e.g. YB_{66} and ZrB_{50}).[35,36] This severely limits their potential applications in

tooling and as abrasives, due to having either boron-rich phases, which can form boride phases with the binder metals, or having the soft lower boride phases (ZrB_2 and YB_6), which hinder the mechanical properties and also reduce the thermal conductivity of the material and as such heat removal from the tool edge.[37]

Metal dodecaborides can be synthesized as single crystals via zone melting, which is not easily scalable.[37] However, using solid solution alloying, it is possible to synthesize a single-phase metal dodecaboride phase, $Zr_{0.5}Y_{0.5}B_{12}$, as confirmed by powder XRD, scanning electron microscopy (SEM) and solid-state NMR spectroscopic data. The fact that these alloys are single phase not only makes it easier to study their properties, but also in case of mechanical properties has the added benefit of solid-solution hardening resulting in enhanced hardness, i.e. 47.6 ± 1.7 GPa at 0.49 N load – a 17 % increase in hardness over the hardness of the parent phases (ZrB_{12} and YB_{12}). Furthermore, we studied the effect of the addition of carbon to the zirconium-yttrium dodecaboride system, as well as provide a possible explanation for the color in metal dodecaborides using diffuse reflectance, XPS, and solid-state NMR (^{10}B and ^{11}B) spectroscopy. Additionally, we studied the magnetic, electronic, and thermal properties of the 50/50 atom% solid solution as well as the parent phases. We show that from one single boride structure, subtle variations of stoichiometry can yield a wide range of outcomes, and that careful optimization of even a few atomic percent can yield optimal properties of a superhard, superconducting boride.

For the purposes of this manuscript: boron carbide ($\sim B_{12-x}C_{2-x}$)[38,39] will be referred to as "B_4C" and zirconium carbide ($\sim ZrC_{1-x}$)[40] as "ZrC".

EXPERIMENTAL PROCEDURES

Pellets of the following nominal compositions: $(Zr_{1-x}Y_x):C_z$:13 B, (x = 0.00, 0.05, 0.25, 0.50, 0.70, 0.75, 0.95 and 1.00; z = 0.0, 0.2, 0.4, 0.5, 0.6, 0.8 and 1.0, C = B_4C + ZrC; 13 boron equivalents account for the evaporation of boron during arc-melting; the amount of pure Zr metal

was adjusted based on the concentration of ZrC, while the total amount of boron was adjusted based on the amount of boron in B_4C), Zr:C_w:13 B and Y:C_w:13 B (w = 1.0, 2.0 and 3.0), ($Zr_{0.5}Y_{0.5}$):Cz:13 B (z = 0.0, 0.2, 0.4, 0.5, 0.6, 0.8 and 1.0 and C = B_4C, ZrC + B_4C and graphite), ($Zr_{1-x}U_x$):20 B, (x = 0.00, 0.05, 0.25, 0.50, 0.70, 0.75, 0.95 and 1.00; metal to boron ratio of 1 : 20 was used in order to conserve uranium metal), Zr:2.5 B, Y:9.0 B, boron carbide, (B_4C):zB (z = 2.5, 6, 9, 16, 22 and 36), zirconium carbide, tungsten carbide were prepared from high-purity metal and boron powders: amorphous boron (99+%, Strem Chemicals, USA), zirconium (99.5%, Strem Chemicals, USA), yttrium (99.9%, Strem Chemicals, USA), depleted uranium metal wire (US Department of Energy), boron carbide (99+%, Strem Chemicals, USA), zirconium carbide (99.5%, Alfa Aesar, USA), tungsten carbide (99.5%, Strem Chemicals, USA) and carbon (graphite, 99+%, Strem Chemicals, USA). In addition, cadmium sulfide (99.999+%, Strem Chemicals, USA), titanium metal (99.9%, Strem Chemicals, USA), chromium metal (99.9%, Strem Chemicals, USA) and potassium permanganate (98%, Alfa Aesar, USA) were used in UV-Vis diffuse-reflectance studies. Additionally, ZB_{12} and YB_{12} samples with a 1 : 20 metal to boron ratio were prepared for SQUID magnetometry analysis.

To ensure homogeneous mixing, the weighted samples were homogenized in a vortex mixer for ~1 minute and pelletized under a load of 10 tons using a hydraulic press (Carver). The pressed pellets were then placed in an arc-melter onto a copper hearth along with oxygen getter materials (zirconium metal). The arc-melter chamber was later sealed and evacuated for 20 minutes followed by purging with argon, this process was repeated 4 times to ensure no oxygen presence in the chamber. During arc-melting, the getters were melted first to ensure the absorbance of any trace oxygen, and then the samples were heated for $T \sim 1$ to 2 minutes at $I \sim$ 145 Amperes until molten, then allowed to solidify, flipped and re-arced 2 times to ensure homogeneity.

The synthesized ingots were split (fractured) into several pieces in a tool steel Plattner style diamond crusher. About half of the total ingot was crushed for PXRD using the diamond crusher into a 325 mesh ($\leqslant$ 45 μm) powder. PXRD was performed on a Bruker D8 Discover powder X-ray diffractometer (Bruker Corporation, Germany) utilizing a CuKα X-ray beam (λ_{ave} = 1.5418 Å, $\lambda_{K\alpha1}$ = 1.5406 Å, $\lambda_{K\alpha2}$ = 1.5444 Å, $\lambda_{K\beta}$ is absorbed by a Ni filter) in the 5 - 100° 2θ range with a scan speed of 0.1055°/s, time per step of 0.3 s. The phases analyzed were cross-referenced against the Joint Committee on Powder Diffraction Standards (JCPDS) database. *Maud* software was used to perform the unit cell refinements.[41–45]

The remaining half of the ingot was epoxidized for Vickers hardness and SEM/EDS measurements using an epoxy/hardener set (Allied High Tech Products Inc., USA), and then polished to an optically flat finish on a semi-automated polisher (Southbay Technology Inc., USA) using both silicon carbide abrasive disks of 120 - 1200 grit (Allied High Tech Products Inc., USA) and 30 - 1 μm particle-size diamond films (Southbay Technology Inc., USA).

The morphology was analyzed using an UltraDry EDS detector (Thermo Scientific, USA) and an FEI Nova 230 high-resolution scanning electron microscope (FEI Company, USA). Vickers hardness testing was performed using a MicroMet 2103 Vickers microhardness tester (Buehler Ltd., USA) with a pyramidal diamond indenter tip. 15 indents were made at applied loads of 0.49, 0.98, 1.96 N each, and a minimum of 10 indents were made at loadings of 2.94 and 4.9 N each, and were performed in random areas of the sample. A high-resolution optical microscope (Zeiss Axiotech 100HD, Carl Zeiss Vision GmbH, Germany) with 500x magnification was used to measure the length of the diagonals of each indent. Vickers hardness (H_v) was calculated using Equation 1:

$$H_v = \frac{1854.4\,F}{a^2} \qquad (1)$$

where F is the loading force applied in Newtons (N), a is the average of the length of the two

diagonals of each indent in micrometers (μm) and H_v is Vickers hardness in gigapascals (GPa).

The reflectance spectra were collected using a diffuse-reflectance attachment on a UV-vis-NIR spectrophotometer (Shimadzu Corp., Japan) in a 400 – 800 nm range (0.5 nm steps) using $BaSO_4$ powder as background. The acquired reflectance spectra was converted to pseudo-absorbance applying Kubelka-Munk theory, using Equation 2:

$$A_p = \log\left(\frac{1-\left(\frac{\%R}{100}\right)^2}{2\left(\frac{\%R}{100}\right)}\right) \quad (2)$$

where %R is the percent reflectance and A_p is the logarithm of the pseudo-absorbance.

XPS spectra were collected using a Kratos Axis Ultra DLD spectrometer equipped with a monochromatic Al Kα X-ray source. Raw data processing was performed using CasaXPS 2.3 software. Spectral binding energies were calibrated by assigning the C 1s peak with a binding energy of 284.5 eV. For high resolution XPS, samples were Ar^+ sputter cleaned at an accelerating voltage of 4 kV.

A Bruker AV III 600 (14.10 Tesla) nuclear magnetic resonance (NMR) spectrometer was employed for the acquisition of ^{11}B and ^{10}B NMR signals at the frequencies of 192.57 MHz (^{11}B) and 64.51 MHz (^{10}B), respectively. Specifically, the ^{11}B and ^{10}B NMR spectroscopic data were acquired by using the magic-angle spinning (MAS) technique. The MAS NMR measurements were performed with the use of a 3.2-mm outside diameter zirconia rotor.[46] The NMR spectra were obtained at several spinning rates, ranging from 5-17 kHz. The boron background effect resulting from the boron nitride stator in the MAS probe was minimized by the use of the "elimination of artifacts in NMR spectroscopy" pulse sequence.[47] For the $^{11,10}B$ saturation recovery measurements with MAS at a rate of 17 kHz, the method of pulsing asynchronously to the spinning sample was applied as initially proposed by Yesinowski, *et al.*[48] All samples were washed in dilute HCl/methanol in order to remove any iron content from powderizing. In addition, all samples were mixed with a small amount of NaCl in order to reduce particle-to-

particle contacts. The ^{11,10}B chemical shift scales were calibrated using the unified Ξ scale,[49] by relating the nuclear shift to the ^{1}H resonance of dilute tetramethylsilane in $CDCl_3$ at a frequency of 600.13 MHz. According to the Ξ scale, the BF_3 etherate compound is the reference for defining zero ppm. The chemical shift referencing was further verified experimentally by acquiring the ^{11,10}B resonance of an aqueous solution of boric acid at pH = 4.4,[50] as well as by measuring a BF_3 etherate sample[49] using a solution state NMR spectrometer (Bruker AV 600). Analysis and simulations of the MAS NMR spectra were performed by using the Solids NMR Models "sola" in the TopSpin software.

Thermal and charge-transport properties were measured from 10 - 300 K using a Physical Property Measurement System (Quantum Design). Arc-melted samples of ZrB_{12} and $Zr_{0.5}Y_{0.5}B_{12}$ were cut and polished into regular shapes. The Seebeck thermopower and thermal conductivity were measured using the Thermal Transport Option in a two-probe configuration. Electrical resistivity was measured using the Alternating Current Transport option and a four-probe geometry with 50 μm Pt wires and Ag paste.

SQUID magnetometry was performed in the 2 – 300 K range initially to narrow down the range of the T_c and in 2 – 10 K range for other samples with a 0.5 K step size using liquid helium on a Quantum Design Magnetic Properties Measurement System (USA). The prepared samples were split into pieces, which could fit into a capsule inserted into a plastic straw. The samples were treated with HCl, washed with ethanol and weighed out before inserting into the magnetometer. The baseline run of the plastic straw was subtracted from the sample signal. All runs were done under an applied field of 10^{-3} Tesla (10 Oersted).[51]

RESULTS AND DISCUSSION

In order to determine the purity and phase composition of the samples, powder X-ray

diffraction (PXRD) and energy-dispersive X-ray spectroscopy (EDS and XPS) were performed. **Figure 2** shows the PXRD spectra for alloys with a nominal composition of $(Zr_{1-x}Y_x)$:13 B, without carbon and with 1 equivalent of carbon in the 15 - 50° 2Θ range (full patterns can be found in **Figure S5** and **S8**). **Figure 3** shows the PXRD spectra for alloys with a nominal composition of $(Zr_{1-x}U_x)$:20 B in the 15 - 50° 2Θ range (full patterns can be found in **Figure S5**). **Figure 4** shows the SEM and optical images of Zr:C_z:13 B and Y:C_z:13 B (z = 1.0, 2.0 and 3.0). **Figure 5** shows the SEM and optical images of $(Zr_{1-x}Y_x)$:13 B, and $(Zr_{1-x}Y_x)$:$C_{1.0}$:13 B. **Figures 6 and 7** show the SEM and optical images, respectively, for the alloys with a composition of $(Zr_{1-x}Y_x)$:C_z:13 B. **Figure 8** show the SEM and optical images for the alloys with a composition of $(Zr_{1-x}U_x)$:20 B. **Figures 9** and **10** show the Vickers hardness data for $(Zr_{1-x}Y_x)$:13 B, without carbon and with 1 equivalent of carbon and $(Zr_{1-x}U_x)$:20 B. **Figure 11** contains contour plots with Vickers hardness data for $(Zr_{1-x}Y_x)$:C_z:13 B. **Figures 12 and 13** contain the XPS surveys for $(Zr_{1-x}Y_x)$:13 B and $(Zr_{1-x}U_x)$:20 B, respectively. **Figure 14** contains diffuse-reflectance UV-Vis spectra for $(Zr_{1-x}Y_x)$:13 B and $(Zr_{1-x}U_x)$:20 B. **Figures 15, 16**, and **17** contain the ^{11}B MAS NMR experimental and simulated spectra, ^{11}B NMR saturation recovery and ^{10}B MAS NMR spectra at 10 and 17 kHz for $(Zr_{1-x}Y_x)$:13 B. Additional PXRD spectra, hardness data and XPS peak fittings can be found in the Supplemental Information file. As mentioned previously, for the purposes of this manuscript boron carbide ($\sim B_{12-x}C_{2-x}$)[38,39] will be referred as "B_4C" and zirconium carbide ($\sim ZrC_{1-x}$)[40] as "ZrC".

Previously, the metal dodecaborides were synthesized with a metal to boron ratio of 1 to 20, in order to prevent the formation of lower boride phases, such as ZrB_2 and YB_6.[26–29] However, in this study we wanted to see whether it is possible to synthesize a single-phase dodecaboride using an almost stoichiometric amount of boron (compensated for the evaporation during arc-melting), similar to the case of WB_4, which has to be synthesized using a metal to

boron ratio of at least 1 to 8.5[19,52–54] in order to prevent the formation of WB_2, but can be prepared as a single-phase compound by substituting in W for ~32 atom% Ta.[19] Indeed it was discovered that a 50/50 atom% solid solution of ZrB_{12} and YB_{12}, prepared with a composition of $(Zr_{0.5}Y_{0.5})$:13 B, is a single-phase compound as confirmed by powder XRD (**Figure 2**) and ^{11}B NMR spectroscopy (**Figure 15**). As can be seen from the PXRD spectra, the amount of secondary lower boride phases, ZrB_2 and YB_6, decreases with the increased amount of secondary metal, and they are suppressed at the eutectic composition, which can be attributed to the formation of a solid solution. ZrB_{12} and YB_{12} are fully soluble in each other (both being cubic-*UB12* structures) and form solid-solutions in the whole range of compositions.[26] This is unsurprising as Zr and Y satisfy all four requirements for solid solution formation according to the Hume-Rothery rules:[55–57] 1) their atomic radii are within ~15 % of each other (r_{Zr} = 1.55 and r_Y = 1.80 Å);[58] 2) they form phases with the same crystal structure (*cubic*-UB_{12});[1] 3) they have similar electronegativities (1.33 and 1.22 for Zr^{4+} and Y^{3+}, respectively);[59,60] and 4) they have similar oxidation states (Zr^{+4} and Y^{+3}).[61] The solid-solution formation is also evident in the change of lattice parameters on going from ZrB_{12} (a = 7.411(6) Å) to YB_{12} (a = 7.502(1) Å), closely following Vegard's law[62] as well as in the EDS values for the yttrium concentration being consistent with the nominal composition (**Table 1**). Furthermore, the formation of the single-phase compound at the 50/50 atom% composition can be seen in the SEM image in **Figure 5** as well as in the results of the NMR spectroscopy discussed later. The ability to synthesize a single phase metal dodecaboride at stoichiometric metal to boron ratios (accounting for boron evaporation during arc-melting) by means of a solid-solution formation allows for a much easier synthesis of possible tools and abrasives and their superior properties due to both solid-solution hardening (mechanical properties) and better thermal conductivity (due to having only grains of one phase).[37] The only other methods for producing a "phase pure" metal dodecaborides are:

having excess boron (M : B = 1 : 20), which results in a considerable amount of boron-rich phases; and zone (induction) melting, although producing single crystals with exact stoichiometry is not easily scalable.[26–29,37]

Upon the addition of carbon to the dodecaboride system, a change in the relative quantity of secondary phases can be observed (**Figure 2**). This is due to the fact that while carbon does form metal borocarbides[63] for low metal to boron ratios (~ 1 : 1), in the case of higher borides and dodecaborides, carbon can be considered an insoluble impurity (**Figure S2**) and as such will preferentially form B_4C, thus reducing the total amount of available boron in the system. However, the addition of carbon has a remarkable effect on the surface morphology of the samples (**Figures 4** and **5**). Carbon has a similar effect to that of zirconium on tungsten tetraboride,[52] in that it causes a rapid cooling and as such very fast nucleation of grains, dramatically reducing their size. This is especially dramatic upon the addition of additional equivalents of carbon, as seen in **Figure 4**, where the lower borides, ZrB_2, and B_4C form a lamellar microstructure pattern resulting from an eutectoid transformation of ZrB_2 and B_4C.[64] As can be seen from **Figure 5**, upon the addition of carbon, the large "white linear" ZrB_2 and "spiral" YB_6 phases are replaced with a large number of smaller grains. The full effect of the addition of carbon on the $(Zr_{1-x}Y_x)$:13 B solid solution can be seen in **Figures 6** and **7**. Note that in the case of ZrB_2, a directional grain growth can be seen, where ZrB_2 and B_4C grains are intermixed, which can be attributed to the high melting points of both ZrB_2 and B_4C (~3230 and ~2450 °C, respectively),[35,38] whereas these phases crystallize before the main dodecaboride phase (~2000 °C)[35,36] and serve as "templates"/nucleation points for the grain growth, similar to the effect of Ti on WB_4.[52]

In order to investigate whether a source of carbon has any effect on the resulting phase/morphology formation, a study was performed where alloys with a nominal composition

of $(Zr_{0.5}Y_{0.5})$:C_z:13 B, where z = 0.2, 0.4, 0.5, 0.8 and 1.0, and the following sources of carbon B_4C, B_4C + ZrC and graphite (**Figures S9** and **S10**). According to the PXRD data in **Figure S9**, in all three cases of different carbon sources, the phase formation is similar, accounting for slight difference in relative intensities of the peaks. Furthermore, optical images in **Figure S10** show that phase formation is indeed independent of the carbon source. Based on these facts, it can be inferred that in the case of ZrC as the carbon source, it dissociates upon melting into zirconium and carbon, which go on to form the metal dodecaboride and boron carbide phases, respectively; B_4C dissociates into boron and carbon and reforms back into boron carbide; and graphitic carbon (and boron) form boron carbide. These results are important because they show that multiple sources of carbon can be used to form the desired phases, resulting in easier synthesis, especially at low concentrations of carbon addition due to the low molecular weight of carbon.

Figure 3 shows the PXRD spectra of $(Zr_{1-x}U_x)$:20 B (1 : 20 metal to boron ratio was used due to the limited amount of U metal), which shows the formation of a solid-solution between ZrB_{12} and UB_{12} (both being *cubic*-UB_{12} structure).[1] The solid-solution formation is also evident in the change of lattice parameters on going from ZrB_{12} (a = 7.411(6) Å) to UB_{12} (a = 7.475(1) Å), closely following Vegard's law[62] as well as in the EDS values for the uranium concentration being consistent with the nominal composition (**Table 1**). **Figure 8** shows the morphology of the dodecaboride phases formed for these alloys, which is similar to cases of other dodecaborides prepared at this metal to boron ratio.[26–29]

Vickers hardness for alloys with a composition of $(Zr_{1-x}Y_x)$:13 B, and $(Zr_{1-x}Y_x)$:$C_{1.0}$:13 B can be seen in **Figure 9**. In both cases a hardness enhancement can be observed upon the increase of the concentration of secondary metal, culminating at the 50/50 atom% composition. In the case of $(Zr_{1-x}Y_x)$:13 B, the hardness increases from 41.6 ± 2.6 and 37.5 ± 4.3 GPa, for Zr:13 B and Y:13 B, respectively, to 47.6 ± 1.7 GPa at 0.49 N load for $(Zr_{0.5}Y_{0.5})$:13 B. The low

hardness of Y:13 B alloy can be attributed to the large amount of the soft YB_6 phase (27.3 ± 1.2 GPa at 0.49 N load, **Figure S11**). This hardness can be attributed to solid-solution hardening effects as outlined by the Hume-Rothery rules discussed above.[55–57] Upon the addition of one equivalent of carbon to $(Zr_{1-x}Y_x)$:13 B, a similar hardness trend can be observed, culminating at the 50/50 atom% composition. The hardness increases from 46.9 ± 3.7 and 37.8 ± 3.3 GPa, for $Zr:C_{1.0}$:13 B and $Y:C_{1.0}$:13 B, respectively, to 48.0 ± 3.8 GPa at 0.49 N load for $(Zr_{0.5}Y_{0.5})$:13 B. Although, with the addition of carbon, the amount of softer secondary phases increases (27.3 ± 1.2 and 26.0 ± 2.7 GPa at 0.49 N for YB_6 and ZrB_2, respectively, **Figure S11**), it is offset by the formation of superhard B_4C (**Figure S11**), resulting in larger error bars (**Figure 9**). A more complete picture of the Vickers hardness change for the $(Zr_{1-x}Y_x):C_z$:13 B system, with the simultaneous variation of both metal and carbon concentrations, can be seen in the 2D contour plots in **Figure 11** (complete list of hardness and error values can be seen in **Table S1**). The general trend in hardness here is that samples near the 50/50 atom% metal composition tend to be the hardest, which can be attributed to intrinsic (solid-solution) and extrinsic (multiple phases ($Zr_{1-x}Y_xB_{12}$, ZrB_2, YB_6 and B_4C) and grain size (Hall-Petch)[65–68]) hardening.

The hardness for the system with the composition $(Zr_{1-x}U_x)$:20 B can be seen in **Figure 10**. Here again solid-solution hardening can be seen for the 50/50 atom% composition, especially when comparing it to pure UB_{12}. The hardness increases from 41.3 ± 1.1[26,28,29] and 28.1 ± 5.3 GPa, for Zr:20 B and U:20 B, respectively, to 43.4 ± 3.1 GPa at 0.49 N load for $(Zr_{0.5}U_{0.5})$:20 B. Again, both zirconium and uranium satisfy the Hume-Rothery[55–57] rules for solid-solutions: 1) atomic size within ~15% (1.55 and 1.75 Å for Zr and U, respectively)[58], 2) ZrB_{12} and UB_{12} crystallize in the same structure (*cubic*-UB_{12}),[1], 3) Zr and U have similar electronegativities (1.33 and 1.38 for Zr and U, respectively),[59,60] and 4) Zr and U have similar oxidation states (Zr^{4+} and $U^{5.5+}$, 5.5+ being a combination of 5+ and 6+).[61]

XPS was used to analyze the oxidation state of the metal and the surface composition of the dodecaboride system. There have been a single attempt to ascertain the oxidation state of the metal in a dodecaboride,[61] and thus is worth revisiting. **Figures 12** and **13** shows XPS survey spectra of $(Zr_{1-x}Y_x)$:13 B and $(Zr_{1-x}U_x)$:20 B systems. The B 1s peak was observed at a binding energy of ~187 eV along with the metal peaks for Zr, Y and U depending on the sample. These spectra also contained O 1s and C 1s peaks due to possible oxidation and surface contaminants. Elemental composition was calculated (**Table 3**) for the metal and boron to compare the varying metal ratios within a system. The atomic percent may not be an accurate representation of the actual composition due to peak overlap of the B 1s and Zr 3d, but can be used to verify relative ratios of the respective metals as already shown through EDS. To investigate the oxidation state of the metals, high-resolution XPS spectra (**Figures S14** and **S15**) were obtained. As an example, $(Zr_{0.50}Y_{0.50})$:13 B was analyzed using high-resolution scans for the Y 3d, B 1s, and Zr 3d peaks. The samples were sputtered with Ar^+ to clean off any surface contaminants prior to these high-resolution scans. A Shirley background was used for peak fitting with spin-orbit splitting clearly observed for Y 3d and Zr 3d. The metallic Y $3d_{5/2}$ and Y $3d_{3/2}$ components at 155.3 and 157.4 eV was observed along with the Y^{3+} components observed at 157.8 and 160.1 eV for Y $3d_{5/2}$ and Y $3d_{3/2}$,[69,70] respectively. The Zr 3d peak also exhibited spin-orbit splitting with the Zr $3d_{5/2}$ and Zr $3d_{3/2}$ at 180.5 and 182.5 eV, respectively, corresponding to Zr^{4+}, and peaks at 178.8 and 181.5 eV corresponding to metallic Zr, which is similar to literature values.[71,72] The high-resolution scan was able to deconvolute B 1s from the Zr 3d peak even though the two peaks were not well resolved in the survey scan. In the instance of $(Zr_{0.25}U_{0.75})$: 20 B (**Figure S15**), a simple peak fitting was done on a high resolution XPS spectra of U 4f peak showing spin-orbit splitting of the U $4f_{7/2}$ and U $4f_{5/2}$ peak. Sputtering of these samples was not needed. The oxidation state of U can be determined by observing the difference in binding energy between the satellite and U $4f_{5/2}$

peak.[73] Due to the low concentration of uranium, the satellite peaks were not easily determined. Our XPS spectra agrees with that of UB_{12} which have previously been analyzed.[74,75] The splitting within the main U $4f_{7/2}$ and U $4f_{5/2}$ peak signals a multivalent state for uranium. Based on previous calculations from high temperature TGA[61] of the oxidation states of uranium, +5 and +6 are the most likely charges on uranium within our system.

Another interesting property of metal dodecaborides is that these phases possess color (**Figures 4, 5, 7** and **8**). The color changes from blue for YB_{12} and violet for ZrB_{12} to metallic for UB_{12}. Although exhibiting color, all dodecaborides are considered to be metals and not semiconductors.[30,76] Therefore, the existence of color can be attributed to a charge transfer (similar to $KMnO_4$, **Figure S13**) from the boron cage to the metal; and changes with the oxidation state of the metal: Y^{3+}, Zr^{4+}, and $U^{5+/6+}$ (**Figure 14**).[61] The diffuse-reflectance spectra for alloys with a composition of $(Zr_{1-x}Y_x)$:13 B (**Figure 14**) show a change in the maxima of pseudo-absorbance (after Kubelka-Munk transformation)[77–82] shift from 594 (ZrB_{12}, violet) to 730 (YB_{12}, blue) nm, closely following Vegard's law[62] values (**Table 1** and **Figures 5** and **14**). For the alloys with a composition $(Zr_{1-x}U_x)$:20 B, upon the addition of 25 atom% U, the samples lose color and behave more like metals[30] (**Figures 8** and **14**).

Figure 15 presents the ^{11}B MAS NMR spectra of $Zr_{1-x}Y_xB_{12}$ compounds (prepared as $(Zr_{1-x}Y_x)$:13 B) at ambient temperature. The spinning rate was 17 kHz, and sufficient to narrow the lineshapes and observe the isotropic shift. Different boron environments will have different chemical shifts and number of resonances in the NMR spectrum. The experimental (**Figure 15, left**) and simulated ^{11}B MAS (**Figure 15, right**) lineshapes are presented in **Figure 15**, where a good agreement between them can be observed. This indicates that in case of ZrB_{12} and YB_{12} additional boron resonances (boron sites) arise at the upfield regime matching to the existence of ZrB_2 (-29 ppm) and YB_6 (2.9 ppm) secondary phases, respectively. Extra boron resonances were

not detected in $Zr_{0.5}Y_{0.5}B_{12}$, which suggests that all the boron atoms in this material have similar chemical environments. As shown in the inset (**Figure 15a**), a systematic ^{11}B resonance shift was detected with the increased yttrium content in the $Zr_{1-x}Y_xB_{12}$ series. Particularly, our data show that the ^{11}B isotropic resonance position for ZrB_{12} that lies around 10 ppm progressively shifts to 16 ppm for $Zr_{0.5}Y_{0.5}B_{12}$ and finally reaches 25 ppm in the case of YB_{12}. The different resonance position of each ^{11}B NMR spectrum verifies that the Y atoms are incorporated into the crystal lattice and, thus, affect the boron bonding environment (**Figure 15b**). Moreover, the entire $Zr_{1-x}Y_xB_{12}$ series is metallic and the downfield resonance shift can arise from the difference in the atomic orbital type (*s*, *p*, *d* states) contributions to the density-of-states at the Fermi level from ZrB_{12} to YB_{12}. Total and partial density-of-states calculations for boron show[83,84] that the dominant contribution originates from 2*p* electrons at the Fermi energy for both compounds, whereas the 2*s* contribution is almost negligible. However, the contributions from the *d*-shells (yttrium 5*d*-states or zirconium 4*d*-states) are also dominant, as well as from the 2*p*-states (boron[84]). The presence of *d*-states amply polarizes the inner *s*-shells, despite the fact that the 2*p* hyperfine interactions are weak compared to *s* and *d* contributions.[85,86] Hence, the observed frequency shift is also proportional to the amount of unpaired *d*-states around the Fermi level due to the admixture of *s*-*d* or *p*-*d* wavefunctions,[86,87] as seen in our case.

The ^{11}B and ^{10}B nuclear spin-lattice relaxation rate ($1/T_1$) measurements are able to explore the band structure and Fermi surface characteristics of $Zr_{1-x}Y_xB_{12}$ series. The T_1 values were given by fitting the saturation recovery data to a single exponential function (**Figure 16**). The ^{11}B T_1 values were 3.12 ± 0.04 s (ZrB_{12}), 4.29 ± 0.01 s ($Zr_{0.5}Y_{0.5}B_{12}$), and 1.34 ± 0.02 s (YB_{12}) at ambient temperature. The metallic nature of the $Zr_{1-x}Y_xB_{12}$ series allows, by using the isotropic shift as obtained from the MAS experiments and the T_1 values at room temperature, to estimate the Korringa ratio,[88] $R \equiv (\frac{K^2 T_1 T}{S})$ as a function of the yttrium concentration. The

experimental values of the Korringa ratios are equal to 0.036 sK (ZrB_{12}), 0.126 sK ($Zr_{0.5}Y_{0.5}B_{12}$), and 0.096 sK (YB_{12}) and are much smaller than unity (evidence for Fermi-contact interaction with *s*- states[88]). This is direct evidence that the detected frequency shift and relaxation process are not governed by *s*-type conduction carriers, but other contributions (*p*- or *d* orbitals) play a dominant role.[86]

In order to investigate the origin of the relaxation mechanism (magnetic or quadrupolar relaxation), we also acquired the ^{10}B NMR spectrum (**Figure 17a**) both at 10 and 17 kHz in order to identify the isotropic resonance as well as to obtain the ^{10}B T_1 value at ambient temperature (**Figure 17b**). By using the ^{10}B and ^{11}B NMR nuclear spin-lattice relaxation data, we can determine the ratios of $\frac{^{10}T_{1M}^{-1}}{^{11}T_{1M}^{-1}}$ and $\frac{^{10}T_{1Q}^{-1}}{^{11}T_{1Q}^{-1}}$, where T_{1M}^{-1} and $T_{1Q}^{-1}$is the magnetic (related to magnetic field fluctuations at the nuclear site) and quadrupolar (related to electric field gradient fluctuations) relaxation rates, respectively.[89,90] The $\frac{^{10}T_{1M}^{-1}}{^{11}T_{1M}^{-1}}$ is related to the square of the magnetogyric ratios $(\frac{\gamma_{10}}{\gamma_{11}})^2$ that is approximately 0.112. On the other hand, the quadrupolar character as given by $\frac{^{10}T_{1Q}^{-1}}{^{11}T_{1Q}^{-1}}$ is related to the ratios of the quadrupole moments, $\frac{Q_{10}^2}{Q_{11}^2} = \frac{2I_{11}+3}{2I_{10}+3} \cdot \frac{I_{10}^2(2I_{10}-1)}{I_{11}^2(2I_{11}-1)} \cdot \frac{T_{1Q(11B)}}{T_{1Q(10B)}}$. The nuclear spin quantum numbers are $I_{10} = 3$ (^{10}B nucleus) and $I_{11} = \frac{3}{2}$ (^{11}B nucleus). Hence, the quadrupolar ratio $\frac{Q_{10}^2}{Q_{11}^2}$ is 4.297, and the $\frac{^{10}T_{1Q}^{-1}}{^{11}T_{1Q}^{-1}}$ is now estimated to be around 0.644. According to the experimental results obtained from the saturation recovery of ^{10}B (**Figure 17b**) and ^{11}B NMR spectroscopic data for the $Zr_{0.5}Y_{0.5}B_{12}$ compound (**Figure 16b**), the ratio of $\frac{^{10}T_1^{-1}}{^{11}T_1^{-1}}$ is equal to 0.089 (a value closer to $(\frac{\gamma_{10}}{\gamma_{11}})^2$), verifying the magnetic character of the nuclear spin-lattice relaxation process. Based on all the aforementioned results, the comparative analysis of the ratio for the two boron isotopes along with the experimental Korringa ratio value

indicates that the boron relaxation process for the $Zr_{0.5}Y_{0.5}B_{12}$ is mainly magnetic and driven by non-*s* states at the Fermi level. This result is in agreement with *ab initio* calculations[83,84] on these dodecaborides, which predicted that the Fermi level is located in the region of a plateau in the density of states that is mainly formed by the boron 2*s* and 2*p* states. In particular, the B 2*p* states [$N_B(E_F)_p \simeq 0.88$ 1/eV cell] were found to be approximately 30 times higher than the B 2*s* states [$N_B(E_F)_s \simeq 0.03$ 1/eV cell[84]]. This is in accordance with the present NMR spectroscopic results, which also verified the major contribution of the non *s*-states at the Fermi level of $Zr_{1-x}Y_xB_{12}$ series.

The magnetic properties of these dodecaborides were assessed with SQUID magnetometry. Curiously, we cannot apply any sort of Vegard's law correlation of T_c to composition, as $Zr_{0.5}Y_{0.5}B_{12}$ ($T_c < 3.5$ K) does not fall between YB_{12} ($T_c \sim 5.0 – 5.5$ K) and ZrB_{12} ($T_c \sim 5.5$ - 6.0 K), but $Zr_{0.95}Y_{0.05}B_{12}$ does (**Figure S16**). The T_c suppression is similar to the one observed for the $Zr_{1-x}Lu_xB_{12}$ system.[91,92] Regardless, from the data, we find that the superconductivity of the dodecaborides persists against the presence of secondary phases, which is not too surprising considering that many dodecaborides are known to possess superconducting transition temperatures in that range.[91–94] However, this is one of the rare cases where a known superhard material is also a superconductor, and $Zr_{0.5}Y_{0.5}B_{12}$ joins $WB_{4.2}$[95] and FeB_4.[96]

Finally, the low temperature thermal and charge-transport properties for ZrB_{12} and $Zr_{0.5}Y_{0.5}B_{12}$ were explored. The room temperature thermal conductivity values for ZrB_{12} (9.24 $W{\cdot}m^{-1}K^{-1}$) and $Zr_{0.5}Y_{0.5}B_{12}$ (9.78 $W{\cdot}m^{-1}K^{-1}$) at 300 K (**Figure 18**) are comparable to other complex borides with similar M:B ratios, such as $Y_{0.56}Al_{0.57}B_{14}$ or $Y_{0.55}B_{14}$ with room temperature thermal conductivities of 7.5 $W{\cdot}m^{-1}K^{-1}$ and 3.1 $W{\cdot}m^{-1}K^{-1}$, respectively.[97] Seebeck coefficients for both materials are low, $< \pm 2$ $\mu V{\cdot}K^{-1}$, indicative of metallic conduction and is supported by our electronic band structure calculations (Figure X band structure/DOS). Previous

Seebeck reports for samples of ZrB_{12} have shown similar magnitudes, but opposite signs indicating differing charge carrier types.[98] This discrepancy could be due to the presence of impurity phases within the samples. Finally, similar to the Seebeck data, both materials exhibit metallic resistivity, increasing to values of 0.398 and 0.536 mΩ·cm for ZrB_{12} and $Zr_{0.5}Y_{0.5}B_{12}$ at 300 K, respectively. Low temperature resistivity data show a superconducting transition for ZrB_{12} (5.35 K) and $Zr_{0.5}Y_{0.5}B_{12}$ (3.58 K). The superconducting transition for ZrB_{12} has been well studied, with reported T_c's ranging from 5.5 to 6.2 K, and falling in-line with our SQUID magnetometry and electrical resistivity data.[76,91,99,100] The resistivity drop for $Zr_{0.5}Y_{0.5}B_{12}$ is much less sharp in comparison to the parent compound, ZrB_{12}, and does not fully drop to a resistivity of 0.

CONCLUSIONS

A single-phase, as evident by PXRD, SEM, and solid-state NMR spectroscopy, metal dodecaboride, $Zr_{0.5}Y_{0.5}B_{12}$, has been synthesized via solid-solution formation. Furthermore, a solid solution of ZrB_{12} and UB_{12} was prepared. The composition and phase purity were established by powder XRD, SEM/EDS, and XPS. The hardness of the $Zr_{0.5}Y_{0.5}B_{12}$ phase is 47.6 ± 1.7 GPa at 0.49 N load, which is ~17% higher compared to its parent compounds, ZrB_{12} and YB_{12}, having a hardness of 41.6 ± 2.6 and 37.5 ± 4.3 GPa, respectively. The hardness of $Zr_{0.5}U_{0.5}B_{12}$ is ~54% higher than that of the UB_{12} parent. In both cases the hardness increase can be attributed to the solid solution hardening effects. In addition, carbon was added to the mixed dodecaboride system. It was found that carbon plays the role of an insoluble impurity and readily forms boron carbide, B_4C, playing a role in "templating" and patterning effects on the resulting surface morphology. Carbon causes the samples to cool down very rapidly and as such nucleates a large number of small grains. It was also found that the source of carbon generates similar

results as far as phase composition and surface morphology. The metal oxidation states were investigated by means of XPS, as a previous determination was done only by fitting high temperature TGA data. The metals were found to be in a +4 state for Zr, a +3 for Y and a +5/+6 state for U. Due to dodecaborides being metals, their color phenomenon was investigated using diffuse-reflectance UV-vis spectroscopy and the color was attributed to the charge transfer from the 24 atom boron cage to the metal, similarly to $KMnO_4$. The color of the $Zr_{1-x}Y_xB_{12}$ solid solution changed from violet for pure ZrB_{12} to blue for YB_{12}; however, for U it was found that upon the addition of 25 atom% U, the color disappears and the sample started to look metallic, suggesting that the corresponding transition had moved beyond the visible region. ^{10}B and ^{11}B solid-state NMR spectroscopy confirmed the cubic structure of the dodecaborides as well as the formation and phase purity of the 50/50 atom% Zr/Y solid solution. Furthermore, it confirmed the metallic character of the dodecaborides and showed that the boron relaxation process for $Zr_{0.5}Y_{0.5}B_{12}$ is mainly magnetic and driven by non-*s* states at the Fermi level. Metal dodecaborides are known superconductors, with a T_c of ~ 5-6 K for ZrB_{12} and YB_{12}, as determined by resistivity and SQUID measurements; however, it was found that the solid solution undergoes a suppression of T_c down to ~ 3 – 3.5 K.

SUPPORTING INFORMATION AVAILABLE

Vickers hardness with errors for $(Zr_{1-x}Y_x):C_z$:13 B, ZrB_2, YB_6, B_4C, ZrC, WC, B_4C in boron, $Zr:C_w$:13 B, $Y:C_w$:13 B; full PXRD spectra for ZrB_2, YB_6, B_4C, ZrC, WC, B_4C in boron, $Zr:C_w$:13 B, $Y:C_w$:13 B, $(Zr_{1-x}Y_x):C_z$:13 B; optical images for $(Zr_{0.5}Y_{0.5}):C_z$:13 B (C = B_4C, ZrC + B_4C, graphite), where x = 0.00, 0.05, 0.25, 0.50, 0.75, 0.95, 1.00, z = 0.0, 0.2, 0.4, 0.5, 0.6, 0.8, 1.0, and w = 1.0, 2.0 and 3.0; diffuse-reflectance data for CdS, Cr-metal and $KMnO_4$; high resolution XPS and peak fitting for $(Zr_{0.5}Y_{0.5})$:13 B and $(Zr_{0.25}U_{0.75})$:20 B; SQUID magnetometry of Zr:13 B, Zr:20B, Y:13 B, Y:20 B and $(Zr_{0.5}Y_{0.5})$:13 B.

CONFLICTS OF INTEREST

There are no conflicts to declare.

ORCID

Georgiy Akopov	0000-0001-9399-9850
Wai H. Mak	0000-0002-8342-1382
Dimitrios Koumoulis	0000-0002-4068-7260
Bryan Owens-Baird	0000-0003-3128-5363
Michael T. Yeung	0000-0002-5677-6970
Paula L. Diaconescu	0000-0003-2732-4155
Julia V. Zaikina	0000-0002-8755-1926
Reza Mohammadi	
Kirill A. Kovnir	0000-0003-1152-1912
Richard B. Kaner	0000-0003-0345-4924

ACKNOWLEDGMENTS

We thank Professor Chong Liu for helpful discussions; and the National Science Foundation Division of Materials Research, Grant DMR-1506860 and the Dr. Myung Ki Hong Endowed Chair in Materials Innovation (R.B.K.), a UCLA Graduate Division Dissertation Year Fellowship and the U.S. Department of Energy, Office of Basic Research, Division of Chemical Sciences, Geosciences, and Biosciences through the Ames Laboratory (G.A.), a UCLA Eugene V. Cota-Robles Fellowship (W.H.M.), the National Science Foundation Grant CHE-1809116 (P.L.D.), and the Virginia Commonwealth University Startup Grant 137422 (R.M.) for financial support. The Ames Laboratory is operated for the U.S. Department of Energy by Iowa State University

under Contract No. DE-AC02-07CH11358. The NMR spectroscopic research is supported by the National Science Foundation MRI program Grant No. 1532232 (R.B.K.). We thank Zachary Hern for help with the uranium metal wire.

REFERENCES

(1) Akopov, G.; Yeung, M. T.; Kaner, R. B. Rediscovering the Crystal Chemistry of Borides. *Adv. Mater.* **2017**, *29*, 1604506.

(2) Lundström, T. Borides: Solid-State Chemistry. In *Encyclopedia of Inorganic Chemistry*; 2006; pp 481–494.

(3) Samsonov, G. V.; Markovskii, L. Y.; Zhigach, A. F.; Valyashko, M. G. *Boron, Its Compounds and Alloys [in Russian]*; House of the Academy of the Sciences Ukrainian SSR: Kiev, 1960.

(4) Samsonov, G. V.; Vinitskii, I. M. *Refractory Compounds [in Russian]*; Atomizdat: Moscow, 1975.

(5) Samsonov, G. V.; Serebriakova, T. I.; Neronov, V. A. *Borides [in Russian]*; Atomizdat: Moscow, 1975.

(6) Buschow, K. H. J. Magnetic Properties of Borides. In *Boron and Refractory Borides*; Matkovich, V. I., Ed.; Springer Berlin Heidelberg: Berlin, 1977; pp 494–515.

(7) Scheifers, J. P.; Zhang, Y.; Fokwa, B. P. T. Boron: Enabling Exciting Metal-Rich Structures and Magnetic Properties. *Acc. Chem. Res.* **2017**, *50*, 2317–2325.

(8) Park, H.; Encinas, A.; Scheifers, J. P.; Zhang, Y.; Fokwa, B. P. T. Boron-Dependency of Molybdenum Boride Electrocatalysts for the Hydrogen Evolution Reaction. *Angew. Chemie - Int. Ed.* **2017**, *56*, 5575–5578.

(9) Jothi, P. R.; Zhang, Y.; Yubuta, K.; Culver, D.; Conley, M. P.; Fokwa, B. P. T. Abundant

Vanadium Diboride with Graphene-like Boron Layers for Hydrogen Evolution. *ACS Appl. Energy Mater.* **2018**, 10.1021/acsaem.8b01615.

(10) Fokwa, B. P. T. Borides: Solid-State Chemistry. *Encycl. Inorg. Bioinorg. Chem.* **2014**, 1–14.

(11) Akopov, G.; Pangilinan, L. E. L. E.; Mohammadi, R.; Kaner, R. B. R. B. Superhard Metal Borides: A Look Forward. *APL Mater.* **2018**, *6*, 070901.

(12) Yeung, M. T.; Mohammadi, R.; Kaner, R. B. Ultraincompressible, Superhard Materials. *Annu. Rev. Mater. Res.* **2015**, *46*, 465–485.

(13) Tergenius, L. E. L. E. Refinement of the Crystal Structure of Orthorhombic Mn2B (Formerly Denoted Mn4B). *J. Less-Common Met.* **1981**, *82*, 335–340.

(14) Yeung, M. T.; Akopov, G.; Lin, C.-W. W.; King, D. J.; Li, R. L.; Sobell, Z. C.; Mohammadi, R.; Kaner, R. B. Superhard $W_{0.5}Ta_{0.5}B$ Nanowires Prepared at Ambient Pressure. *Appl. Phys. Lett.* **2016**, *109*, 203107.

(15) Yeung, M. T.; Lei, J.; Mohammadi, R.; Turner, C. L.; Wang, Y.; Tolbert, S. H.; Kaner, R. B. Superhard Monoborides: Hardness Enhancement through Alloying in W1−xTaxB. *Adv. Mater.* **2016**, *28*, 6993–6998.

(16) Post, B.; Glaser, F. W.; Moskowitz, D. Transition Metal Diborides. *Acta Metall.* **1954**, *2*, 20–25.

(17) Pangilinan, L. E.; Turner, C. L.; Akopov, G.; Anderson, M.; Mohammadi, R.; Kaner, R. B. Superhard Tungsten Diboride-Based Solid Solutions. *Inorg. Chem.* **2018**, *57*, 15305–15313.

(18) Knappschneider, A.; Litterscheid, C.; Brgoch, J.; George, N. C.; Henke, S.; Cheetham, A. K.; Hu, J. G.; Seshadri, R.; Albert, B. Manganese Tetraboride, MnB<inf>4</Inf>: High-Temperature Crystal Structure, p-n Transition, ^{55}Mn NMR Spectroscopy, Solid Solutions,

and Mechanical Properties. *Chem. - A Eur. J.* **2015**, *21*, 8177–8181.

(19) Akopov, G.; Roh, I.; Sobell, Z. C.; Yeung, M. T. M. T.; Pangilinan, L.; Turner, C. L. C. L.; Kaner, R. B. R. B. Effects of Variable Boron Concentration on the Properties of Superhard Tungsten Tetraboride. *J. Am. Chem. Soc.* **2017**, *139*, 17120–17127.

(20) Akopov, G.; Yeung, M. T.; Roh, I.; Sobell, Z. C.; Yin, H.; Mak, W. H.; Khan, S. I.; Kaner, R. B. Effects of Dodecaboride-Forming Metals on the Properties of Superhard Tungsten Tetraboride. *Chem. Mater.* **2018**, *30*.

(21) La Placa, S.; Binder, I.; Post, B. Binary Dodecaborides. *J. Inorg. Nucl. Chem.* **1961**, *18*, 113–117.

(22) Tanaka, T.; Otani, S.; Ishizawa, Y. Preparation of Single Crystals of YB66. *J. Cryst. Growth* **1985**, *73*, 31–36.

(23) Crespo, A. J.; Tergenius, L. E.; Lundström, T. The Solid Solution of 4d, 5d and Some p Elements in β Rhombohedral Boron. *J. Less-Common Met.* **1981**, *77*, 147–150.

(24) Andersson, S.; Lundström, T. The Solubility of Chromium in β-Rhombohedral Boron as Determined in CrB∼41 by Single-Crystal Diffractometry. *J. Solid State Chem.* **1970**, *2*, 603–611.

(25) Akopov, G.; Yin, H.; Roh, I.; Pangilinan, L. E.; Kaner, R. B. Investigation of Hardness of Ternary Borides of the YCrB4,Y2ReB6, Y3ReB7, and YMo3B7 Structural Types. *Chem. Mater.* **2018**, *30*, 6494–6502.

(26) Akopov, G.; Yeung, M. T.; Sobell, Z. C.; Turner, C. L.; Lin, C. W.; Kaner, R. B. Superhard Mixed Transition Metal Dodecaborides. *Chem. Mater.* **2016**, *28*, 6605–6612.

(27) Akopov, G.; Yeung, M. T.; Turner, C. L.; Li, R. L.; Kaner, R. B. Stabilization of HfB12 in Y1-XHfxB12 under Ambient Pressure. *Inorg. Chem.* **2016**, *55*, 5051–5055.

(28) Akopov, G.; Roh, I.; Sobell, Z. C.; Yeung, M. T. M. T.; Kaner, R. B. R. B. Investigation of

Ternary Metal Dodecaborides (M1M2M3)B12 (M1, M2 and M3 = Zr, Y, Hf and Gd). *Dalton Trans.* **2018**, *47*, 6683–6691.

(29) Akopov, G.; Sobell, Z. C.; Yeung, M. T.; Kaner, R. B. Stabilization of LnB12 (Ln = Gd, Sm, Nd, and Pr) in Zr(1– x)Ln(x)B12 under Ambient Pressure. *Inorg. Chem.* **2016**, *55*, 12419–12426.

(30) Troć, R.; Wawryk, R.; Pikul, A.; Shitsevalova, N. Physical Properties of Cage-like Compound UB12. *Philos. Mag.* **2015**, *95*, 2343–2363.

(31) Paderno, Y.; Shitsevalova, N. Stabilization of Cubic Scandium Dodecaboride. *J. Alloys Compd.* **1995**, *219*, 119–123.

(32) Hamada, K.; Wakata, M.; Sugii, N.; Matsuura, K.; Kubo, K.; Yamauchi, H. Structural Phase Transition in the Zr1−xScxB12 System. *Phys. B Condens. Matter* **1994**, *194–196*, *P*, 443–444.

(33) Cannon, J. F.; Cannon, D. M.; Tracy Hall, H. High Pressure Syntheses of SmB2 and GdB12. *J. Less-Common Met.* **1977**, *56*, 83–90.

(34) Cannon, J. F.; Farnsworth, P. B. High Pressure Syntheses of ThB12 and HfB12. *J. Less Common Met.* **1983**, *92*, 359–368.

(35) Portnoi, K. I. I.; Romashev, V. M.; Burobina, L. N.; Romashov, V. M.; Burobina, L. N. Constitution Diagram of the System Zirconium-Boron. *Powder Metall. Met. Ceram.* **1970**, *7*, 68–71.

(36) Liao, P. K.; Spear, K. E. The B-Y (Boron-Yttrium) System. *J. Phase Equilib.* **1995**, *16*, 521–524.

(37) Paderno, Y. B.; Adamovskii, A. A.; Lyashchenko, A. B.; Paderno, V. N.; Fillipov, V. B.; Naydich, Y. V. Zirconium Dodecaboride-Based Cutting Material. *Powder Metall. Met. Ceram.* **2004**, *43*, 546–548.

(38) Okamoto, H. B-C (Boron-Carbon). *J. Phase Equilibria* **1992**, *13*, 436.

(39) Sologub, O.; Michiue, Y.; Mori, T. Boron Carbide, B13-x C2-y (x = 0.12, y = 0.01). *Acta Crystallogr. Sect. E Struct. Reports Online* **2012**, *68*, 1–6.

(40) Okamoto, H. C-Zr (Carbon-Zirconium). *J. Phase Equilibria* **1996**, *17*, 162.

(41) Lutterotti, L.; Matthies, S.; Wenk, H. R.; Schultz, A. S.; Richardson, J. W. Combined Texture and Structure Analysis of Deformed Limestone from Time-of-Flight Neutron Diffraction Spectra. *J. Appl. Phys.* **1997**, *81*, 594–600.

(42) Lutterotti, L.; Chateigner, D.; Ferrari, S.; Ricote, J. Texture, Residual Stress and Structural Analysis of Thin Films Using a Combined X-Ray Analysis. *Thin Solid Films* **2004**, *450*, 34–41.

(43) Lutterotti, L.; Bortolotti, M.; Ischia, G.; Lonardelli, I.; Wenk, H. R. Rietveld Texture Analysis from Diffraction Images. *Zeitschrift fur Krist. Suppl.* **2007**, *1*, 125–130.

(44) Lutterotti, L. Maud Rev. 2.55. *Univ. Trento-Italy, Dep. Ind. Eng. Trento, Italy* **2015**.

(45) Lutterotti, L. Total Pattern Fitting for the Combined Size-Strain-Stress-Texture Determination in Thin Film Diffraction. *Nucl. Instruments Methods Phys. Res. Sect. B Beam Interact. with Mater. Atoms* **2010**, *268*, 334–340.

(46) Turner, C. L.; Zujovic, Z.; Koumoulis, D.; Taylor, R. E.; Kaner, R. B. Microscopic Investigation of Local Structural and Electronic Properties of Tungsten Tetraboride: A Superhard Metallic Material. *J. Mater. Sci.* **2019**, *54*, 3547–3557.

(47) Jaeger, C.; Hemmann, F. EASY: A Simple Tool for Simultaneously Removing Background, Deadtime and Acoustic Ringing in Quantitative NMR Spectroscopy. Part II: Improved Ringing Suppression, Application to Quadrupolar Nuclei, Cross Polarisation and 2D NMR. *Solid State Nucl. Magn. Reson.* **2014**, *63*, 13–19.

(48) Yesinowski, J. P. Finding the True Spin-Lattice Relaxation Time for Half-Integral Nuclei

with Non-Zero Quadrupole Couplings. *J. Magn. Reson.* **2015**, *252*, 135–144.

(49) Harris, R. K.; Becker, E. D.; Cabral De Menezes, S. M.; Goodfellow, R.; Granger, P. NMR Nomenclature: Nuclear Spin Properties and Conventions for Chemical Shifts (IUPAC Recommendations 2001). *Concepts Magn. Reson. Part A Bridg. Educ. Res.* **2002**, *14*, 326–346.

(50) Bishop, M.; Shahid, N.; Yang, J.; Barron, A. R. Determination of the Mode and Efficacy of the Cross-Linking of Guar by Borate Using MAS11B NMR of Borate Cross-Linked Guar in Combination with Solution11B NMR of Model Systems. *Dalton Trans.* **2004**, No. 17, 2621–2634.

(51) Renosto, S. T.; Corrêa, L. E.; da Luz, M. S.; Rosa, P. F. S.; Fisk, Z.; Albino-Aguiar, J.; Machado, A. J. S. Superconductivity in the Th0.93Zr0.07B12 Compound with UB12 Prototype Structure. *Phys. Lett. A* **2015**, *379*, 2498–2501.

(52) Akopov, G.; Yeung, M. T.; Turner, C. L.; Mohammadi, R.; Kaner, R. B. Extrinsic Hardening of Superhard Tungsten Tetraboride Alloys with Group 4 Transition Metals. *J. Am. Chem. Soc.* **2016**, *138*, 5714–5721.

(53) Akopov, G.; Yeung, M. T.; Roh, I.; Sobell, Z. C.; Yin, H.; Mak, W. H.; Khan, S. I.; Kaner, R. B. Effects of Dodecaboride Forming Metals on the Properties of Superhard Tungsten Tetraboride. *Chem. Mater.* **2018**, *30*, 3559–3570.

(54) Mohammadi, R.; Xie, M.; Lech, A. T.; Turner, C. L.; Kavner, A.; Tolbert, S. H.; Kaner, R. B. Toward Inexpensive Superhard Materials: Tungsten Tetraboride-Based Solid Solutions. *J. Am. Chem. Soc.* **2012**, *134*, 20660–20668.

(55) Hume-Rothery, W.; Powell, H. M. On the Theory of Super-Lattice Structures in Alloys. *Z. Krist.* **1935**, *91*, 23.

(56) Hume-Rothery, W.; Smallman, R. W.; Haworth, C. W. *The Structure of Metals and Alloys*;

The Institute of Metals: London, 1969.

(57) Hume-Rothery, W. *Atomic Theory for Students of Metallurgy*, 5th ed.; The Institute of Metals: London, 1969.

(58) Slater, J. C. Atomic Radii in Crystals. *J. Chem. Phys.* **1964**, *41*, 3199–3204.

(59) Pauling, L. The Nature of the Chemical Bond. IV. The Energy of Single Bonds and the Relative Electronegativity of Atoms. *J. Am. Chem. Soc.* **1932**, *54*, 3570–3582.

(60) Pauling, L. *Nature of the Chemical Bond*, 3rd ed.; Cornell University Press: Ithaca, 1960.

(61) Mar, R. W.; Stout, N. D. High Temperature Enthalpies of Binary Dodecaborides. *J. Chem. Phys.* **1972**, *57*, 5342–5349.

(62) Vegard, L. Die Konstitution Der Mischkristalle Und Die Raumfullung Der Atome. *Zeitschrift fur Phys.* **1921**, *5*, 17–26.

(63) Mansouri Tehrani, A.; Oliynyk, A. O.; Parry, M.; Rizvi, Z.; Couper, S.; Lin, F.; Miyagi, L.; Sparks, T. D.; Brgoch, J. Machine Learning Directed Search for Ultraincompressible, Superhard Materials. *J. Am. Chem. Soc.* **2018**, *140*, 9844–9853.

(64) McCaughey, C.; Tsakiropoulos, P. Type of Primary Nb5Si3and Precipitation of Nbssin ANb5Si3in a Nb-8.3Ti-21.1Si-5.4Mo-4W-0.7Hf (atom%) near Eutectic Nb-Silicide-Based Alloy. *Materials (Basel).* **2018**, *11*, 1–25.

(65) Li, Y.; Bushby, A. J.; Dunstan, D. J. The Hall–Petch Effect as a Manifestation of the General Size Effect. *Proc. R. Soc. A Math. Phys. Eng. Sci.* **2016**, *472*, 20150890.

(66) Petch, N. J. The Cleavage Strength of Polycrystals. *J. Iron Steel Inst.* **1953**, *174*, 25–28.

(67) Bundy, F. P.; Hall, H. T.; Strong, H. M.; Wentorf, R. H. Man-Made Diamonds. *Nature* **1955**, *176*, 51–55.

(68) Bovenkerk, H. P.; Bundy, F. P.; Hall, H. T.; Strong, H. M.; Wentorf, R. H. Preparation of Diamond. *Nature* **1959**, *184*, 1094–1098.

(69) Uwamino, Y.; Ishizuka, T.; Yamatera, H. X-Ray Photoelectron Compounds Spectroscopy of Rare-Earth. *J. Electron Spectros. Relatom Phenomena* **1984**, *34*, 67–78.

(70) Baba, Y.; Sasaki, T. A. Application of X-ray-induced Auger Electron Spectroscopy to State Analyses of Hydrogen Implanted in Y, Zr and Nb Metals. *Surf. Interface Anal.* **1984**, *6*, 171–173.

(71) Anderson, J. A.; Fierro, J. L. G. Bulk and Surface Properties of Copper-Containing Oxides of the General Formula LaZr1-XCuxO3. *Journal of Solid State Chemistry*. 1994, pp 305–313.

(72) Nishino, Y.; Krauss, A. R.; Lin, Y.; Gruen, D. M. Initial Oxidation of Zirconium and Zircaloy-2 with Oxygen and Water Vapor at Room Temperature. *J. Nucl. Mater.* **1996**, *228*, 346–353.

(73) Ilton, E. S.; Bagus, P. S. XPS Determination of Uranium Oxidation States. *Surf. Interface Anal.* **2011**, *43*, 1549–1560.

(74) Samsel-Czekała, M.; Talik, E.; Troć, R.; Shitsevalova, N. Electronic Structure of Cage-like Compound UB12 - Theory and XPS Experiment. *J. Alloys Compd.* **2014**, *615*, 446–450.

(75) Ejima, T.; Sato, S.; Suzuki, S.; Saito, Y.; Fujimori, S.; Sato, N.; Kasaya, M.; Komatsubara, T.; Kasuya, T.; Ōnuki, Y. Line Shapes of the XPS U 4f Spectra in Some Uranium Compounds. *Phys. Rev. B - Condens. Matter Mater. Phys.* **1996**, *53*, 1806–1813.

(76) Ma, T.; Li, H.; Zheng, X.; Wang, S.; Wang, X.; Zhao, H.; Han, S.; Liu, J.; Zhang, R.; Zhu, P.; et al. Ultrastrong Boron Frameworks in ZrB12: A Highway for Electron Conducting. *Adv. Mater.* **2017**, *29*, 1–7.

(77) Tauc, J.; Menth, A. States in the Gap. *J. Non. Cryst. Solids* **1972**, *8–10*, 569–585.

(78) Tauc, J. Optical Properties and Electronic Structure of Amorphous Ge and Si. *Mater. Res.*

Bull. **1968**, *3*, 37–46.

(79) Tauc, J.; Grigorovici, R.; Vancu, A. Optical Properties and Electronic Structure of Amorphous Germanium. *Phys. Status Solidi* **1966**, *15*, 627–637.

(80) Hecht, H. G. The Interpretation of Diffuse Reflectance Spectra. *J. Res. Natl. Bur. Stand. A* **1976**, *80*, 567–583.

(81) Kubelka, P. New Contributions to the Optics of Intensely Light-Scattering Materials Part II: Nonhomogeneous Layers*. *J. Opt. Soc. Am.* **1948**, *38*, 330–335.

(82) Kubelka, P.; Munk, F. Ein Beitrag Zur Optik Der Farbanstiche. *Z. Techn. Phys.* **1931**, *12*, 593–601.

(83) Korozlu, N.; Surucu, G. The Electronic and Optical Properties of MB12 (M = Zr, Hf, Y, Lu) Dodecaboride Compounds. *Phys. Scr.* **2013**, *87*.

(84) Shein, I. R.; Ivanovskii, A. L. Band Structure of Superconducting Dodecaborides YB12 and ZrB12. *Phys. Solid State* **2003**, *45*, 1429–1434.

(85) Papavassiliou, G.; Pissas, M.; Karayanni, M.; Fardis, M.; Koutandos, S.; Prassides, K. 11B and 27Al NMR Spin-Lattice Relaxation and Knight Shift of Mg(1-x)Al(x)B2 Evidence for an Anisotropic Fermi Surface. *Phys. Rev. B - Condens. Matter Mater. Phys.* **2002**, *66*, 1–4.

(86) Winter, J. *Magnetic Resonance in Metals*, xiii.; Claredon Press: Oxford, 1971.

(87) Carter, G. C.; Bennett, L. H.; Kahan, D. J. *Metallic Shifts in NMR : A Review of the Theory and Comprehensive Critical Data Compilation of Metallic Materials: Part 2, Progress in Materials Science (Book 20)*, 1st ed.; Pergamon Press: Oxford, 1977.

(88) Suh, B. J.; Zong, X.; Singh, Y.; Niazi, A.; Johnston, D. C. B11 NMR in the Layered Diborides Os B2 and Ru B2. *Phys. Rev. B - Condens. Matter Mater. Phys.* **2007**, *76*, 1–4.

(89) Balz, R.; Brändie, U.; Kammerer, E.; Köhnlein, D.; Lutz, O.; Nolle, A.; Schafitel, R.; Veil,

E. 11B and 10B NMR Investigations in Aqueous Solutions. *Zeitschrift fur Naturforsch. - Sect. A J. Phys. Sci.* **1986**, *41*, 737–742.

(90) Brinkmann, D. Quadrupolar Relaxation - What Would We Do without It in High-Tc Superconductor Studies? *Zeitschrift fur Naturforsch. - Sect. A J. Phys. Sci.* **2000**, *55*, 323–326.

(91) Teyssier, J.; Lortz, R.; Petrovic, A.; Van Der Marel, D.; Filippov, V.; Shitsevalova, N. Effect of Electron-Phonon Coupling on the Superconducting Transition Temperature in Dodecaboride Superconductors: A Comparison of LuB12with ZrB12. *Phys. Rev. B - Condens. Matter Mater. Phys.* **2008**, *78*, 1–7.

(92) Sluchanko, N. E.; Azarevich, A. N.; Anisimov, M. A.; Bogach, A. V.; Gavrilkin, S. Y.; Gilmanov, M. I.; Glushkov, V. V.; Demishev, S. V.; Khoroshilov, A. L.; Dukhnenko, A. V.; et al. Suppression of Superconductivity in Lux Zr1-x B12: Evidence of Static Magnetic Moments Induced by Nonmagnetic Impurities. *Phys. Rev. B* **2016**, *93*, 1–7.

(93) Ge, J. Y.; Gladilin, V. N.; Sluchanko, N. E.; Lyashenko, A.; Filipov, V. B.; Indekeu, J. O.; Moshchalkov, V. V. Paramagnetic Meissner Effect in ZrB12single Crystal with Non-Monotonic Vortex-Vortex Interactions. *New J. Phys.* **2017**, *19*.

(94) Thakur, S.; Biswas, D.; Sahadev, N.; Biswas, P. K.; Balakrishnan, G.; Maiti, K. Complex Spectral Evolution in a BCS Superconductor, ZrB 12. *Sci. Rep.* **2013**, *3*, 3–8.

(95) Carnicom, E. M.; Strychalska-Nowak, J.; Wiśniewski, P.; Kaczorowski, D.; Xie, W.; Klimczuk, T.; Cava, R. J. Superconductivity in the Superhard Boride WB4.2. *Supercond. Sci. Technol.* **2018**, *31*.

(96) Gou, H.; Dubrovinskaia, N.; Bykova, E.; Tsirlin, A. A.; Kasinathan, D.; Schnelle, W.; Richter, A.; Merlini, M.; Hanfland, M.; Abakumov, A. M.; et al. Discovery of a Superhard Iron Tetraboride Superconductor. *Phys. Rev. Lett.* **2013**, *111*, 157002.

(97) Maruyama, S.; Miyazaki, Y.; Hayashi, K.; Kajitani, T.; Mori, T. Excellent P-n Control in a High Temperature Thermoelectric Boride. *Appl. Phys. Lett.* **2012**, *101*.

(98) Glushkov, V.; Ignatov, M.; Demishev, S.; Filippov, V.; Flachbart, K.; Ishchenko, T.; Kuznetsov, A.; Samarin, N.; Shitsevalova, N.; Sluchanko, N. Phonon Drag Induced by Einstein Mode in ZrB12. *Phys. Status Solidi Basic Res.* **2006**, *243*, 72–74.

(99) Lortz, R.; Wang, Y.; Abe, S.; Meingast, C.; Paderno, Y. B.; Filippov, V.; Junod, A. Specific Heat, Magnetic Susceptibility, Resistivity and Thermal Expansion of the Superconductor ZrB12. *Phys. Rev. B - Condens. Matter Mater. Phys.* **2005**, *72*, 1–8.

(100) Daghero, D.; Gonnelli, R. S.; Ummarino, G. A.; Calzolari, A.; Dellarocca, V.; Stepanov, V. A.; Filippov, V. B.; Paderno, Y. B. Andreev-Reflection Spectroscopy in ZrB12 Single Crystals. *Supercond. Sci. Technol.* **2004**, *17*.

(101) Leithe-Jasper, A.; Sato, A.; Tanaka, T. Refinement of the Crystal Structure of Zirconium Dodecaboride, ZrB12, at 140 K and 293 K. *Zeitschrift fur Krist. - New Cryst. Struct.* **2002**, *217*, 319–320.

(102) Matkovich, V. I.; Economy, J.; Giese, R. F.; Barrett, R. The Structure of Metallic Dodecarborides. *Acta Crystallogr.* **1965**, *19*, 1056–1058.

(103) Callmer, B. A Single-Crystal Diffractometry Boron Investigation of Scandium in Beta-Rhombohedral Boron. *J. Solid State Chem.* **1978**, *23*, 391–398.

Table 1. Unit Cell Parameters[a,b], Relative Concentration (EDS) of Y in $(Zr_{1-x}Y_x)$:13 B and U in $(Zr_{1-x}U_x)$:20 B Alloys and Peak Maxima (Diffuse-Reflectance) for $(Zr_{1-x}Y_x)$:13 B.

Nominal atom % of Y or U	$(Zr_{1-x}Y_x)$:13 B					$(Zr_{1-x}U_x)$:20 B		
	$a_{(XRD)}$[a] (Å)	$a_{(Veg)}$[b] (Å)	atom %Y (EDS)	λ_{meas}[f] (nm)	$\lambda_{Veg.}$ (nm)	$a_{(XRD)}$[a] (Å)	$a_{(Veg)}$[b] (Å)	atom %U (EDS)
0	7.411(6)	7.404[c]	-	594	594	7.409(7)	7.404[c]	-
5	7.414(4)	7.409	5.0 ± 0.5	601	601	7.414(4)	7.407	8.1 ± 0.4
25	7.426(1)	7.428	25.8 ± 2.1	630	628	7.428(3)	7.421	31.8 ± 0.7
50	7.453(1)	7.452	49.1 ± 1.5	652	662	7.447(8)	7.439	56.1 ± 1.3
75	7.472(1)	7.476	73.4 ± 2.0	700	696	7.463(5)	7.456	79.2 ± 4.3
95	7.487(6)	7.495	91.0 ± 3.9	715	723	7.473(6)	7.470	95.3 ± 7.8
100	7.502(1)	7.500[d]	-	730	730	7.475(1)	7.473[e]	-

[a]From cell refinement using *Maud*,[41–45] error in parenthesis;
[b]Calculated using Vegard's Law:[62]
[c]Literature value for cell of ZrB_{12}: a = 7.404 Å (ICSD (Inorganic Crystal Structure Database) 409634):[101]
[d]Literature value for cell of YB_{12}: a = 7.500 Å (ICSD 23860);[102]
[e]Literature value for cell of UB_{12}: a = 7.473 Å (ICSD 23862);[102]
[f]Determined from UV-vis diffuse-reflectance analysis.

Table 2. Unit Cell Parameters[a] and Relative Concentration (EDS) of Y in $(Zr_{1-x}Y_x):C_z$:13 B Alloys

Nominal atom % of C/Y		Nominal concentration of yttrium in $Zr_{1-x}Y_x:C_z$:13 B (atom% Y)						
		0	5	25	50	75	95	100
Nominal concentration of carbon in $Zr_{1-x}Y_x:C_z$:13 B (atom% C)	0	7.411(6)	7.414(4)	7.426(1)	7.453(1)	7.472(1)	7.487(6)	7.502(1)
		-	5.0 ± 0.5	25.8 ± 2.1	49.1 ± 1.5	73.4 ± 2.0	91.0 ± 3.9	-
	20	7.404(5)	7.417(7)	7.434(7)	7.460(8)	7.476(5)	7.499(5)	7.501(5)
		-	6.0 ± 0.4	27.3 ± 0.6	52.3 ± 1.1	73.7 ± 1.5	80.2 ± 2.2	-
	40	7.405(2)	7.416(6)	7.442(1)	7.460(5)	7.463(1)	7.497(8)	7.500(1)
		-	8.4 ± 0.4	35.1 ± 0.6	49.4 ± 1.3	68.9 ± 1.3	86.1 ± 3.4	-
	50	7.404(1)	7.410(7)	7.434(1)	7.461(2)	7.462(4)	7.490(3)	7.505(1)
		-	6.0 ± 0.4	25.3 ±1.2	52.2 ± 0.6	56.3 ± 0.8	88.7 ± 5.1	-
	60	7.411(1)	7.419(8)	7.445(2)	7.465(4)	7.454(5)	7.497(3)	7.500(2)
		-	7.4 ± 0.4	36.7 ± 0.8	49.2 ± 0.6	58.5 ± 1.6	90.7 ± 3.8	-
	80	7.409(6)	7.416(7)	7.441(1)	7.459(4)	7.456(6)	7.490(6)	7.498(8)
		-	11.3 ± 0.3	36.7 ± 0.9	53.4 ± 2.0	52.3 ± 0.7	92.9 ± 2.7	-
	100	7.405(1)	7.414(4)	7.454(1)	7.459(5)	7.454(1)	7.481(2)	7.496(1)
		-	11.1 ± 0.3	28.4 ± 1.6	49.7 ±1.2	53.5 ± 3.3	95.1 ± 5.5	-

[a]From cell refinement using *Maud*,[41–45] error in parenthesis.

Table 3. Concentration (XPS) of Y in ($Zr_{1-x}Y_x$):13 B and U in ($Zr_{1-x}U_x$):20 B Alloys

Nominal Composition	Absolute Composition			Y 3p (relative[b] atom%)	Nominal Composition	Absolute Composition			U 4f (relative[b] atom%)
	Zr 3p (atom %)	Y 3p (atom %)	B 1s (atom %)			Zr 3p (atom %)	U 4f (atom %)	B 1s (atom %)	
Zr:13 B	3.39	-	96.61	-	-	-	-	-	-
($Zr_{0.95}Y_{0.05}$):13 B	3.49	[a]	96.51	[a]	($Zr_{0.95}U_{0.05}$):20 B	2.50	0.52	96.98	17.2
($Zr_{0.75}Y_{0.25}$):13 B	2.83	1.14	96.03	28.7	($Zr_{0.75}U_{0.25}$):20 B	2.41	1.17	96.41	32.6
($Zr_{0.50}Y_{0.50}$):13 B	2.17	2.36	95.47	52.1	($Zr_{0.50}U_{0.50}$):20 B	2.40	1.61	95.99	40.1
($Zr_{0.25}Y_{0.75}$):13 B	1.68	4.47	93.85	72.6	($Zr_{0.25}U_{0.75}$):20 B	0.92	1.67	97.40	64.5
($Zr_{0.05}Y_{0.95}$):13 B	[a]	5.57	94.43	[a]	($Zr_{0.05}U_{0.95}$):20 B	[a]	5.35	94.65	[a]
Y:13 B	-	9.26	90.74	-	U:20 B	-	6.04	93.96	-

[a]Peak not visible due to low concentration;
[b]Calculated from the absolute metal composition.

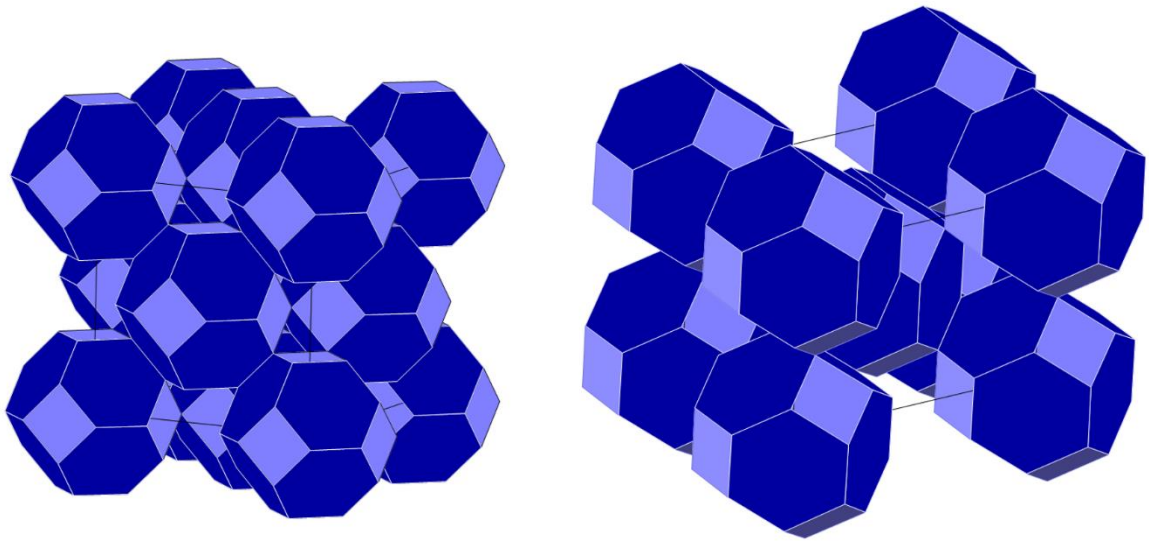

Figure 1. (Left) Polyhedra model of the unit cell of a cubic-UB_{12} (ZrB_{12}, $Fm\bar{3}m$, ICSD 409634)[101] structural type metal dodecaboride; **(right)** polyhedra model of the unit cell of a tetragonal-ScB_{12} (ScB_{12}, *I4/mmm*, JCPDS 00-024-1014)[103] structural type metal dodecaboride. "Reprinted (adapted) with permission from (Akopov, G., Sobell, Z.C., Yeung, M.T., and Kaner, R.B. *Inorganic Chemistry* **2016** *55* (23), 12419-12426 DOI: 10.1021/acs.inorgchem.6b02311). Copyright (2016) American Chemical Society."

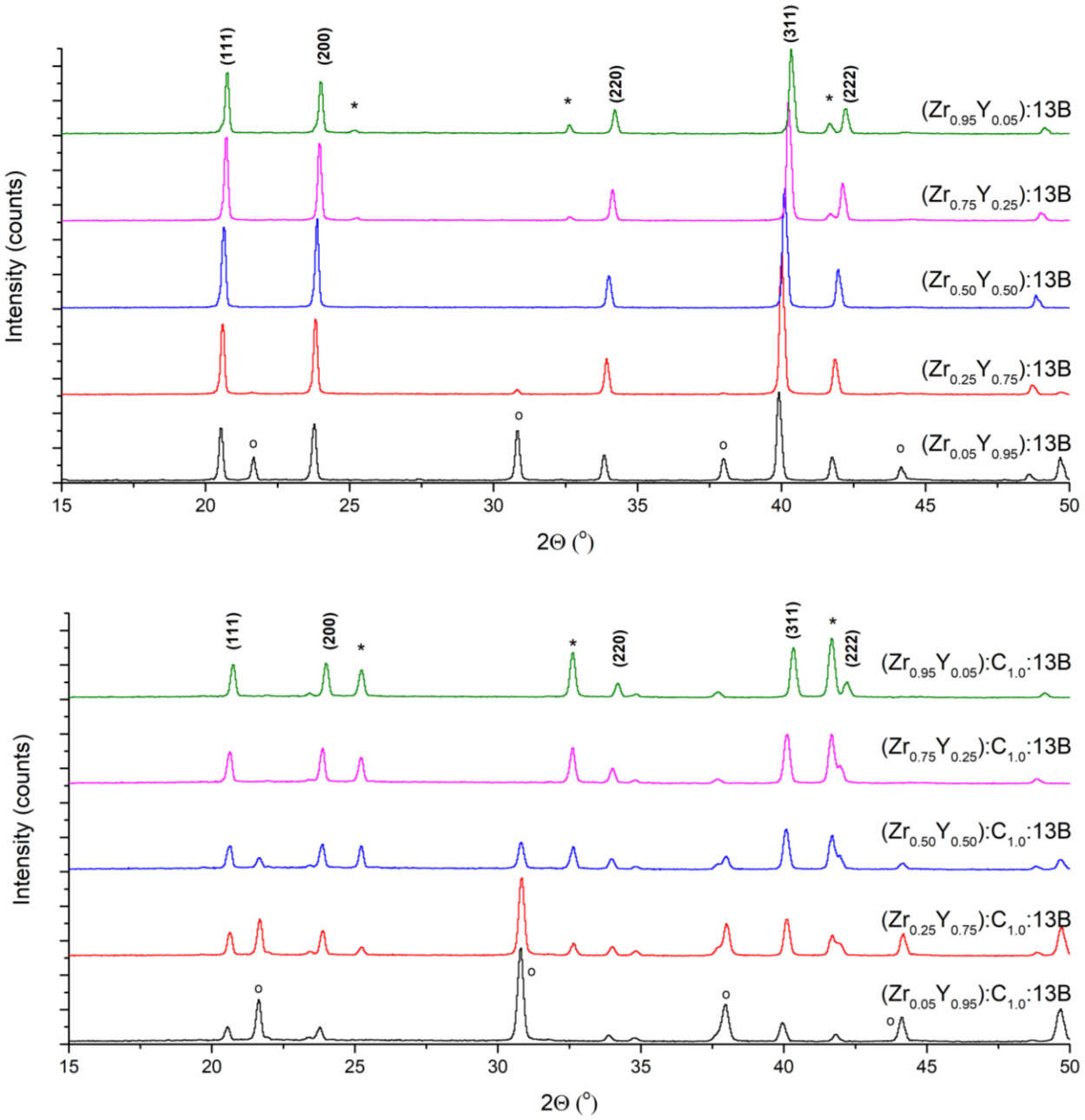

Figure 2. Powder XRD patterns of alloys with a composition of: **(top)** $(Zr_{1-x}Y_x)$:13 B, and **(bottom)** $(Zr_{1-x}Y_x):C_{1.0}$:13 B, where x = 0.05, 0.25, 0.50, 0.75 and 0.95. The peaks were assigned using YB_{12} ($Fm\bar{3}m$, JCPDS 01-073-1382), ZrB_2 (*P6/mmm*, JCPDS 00-034-0423, indicated by (*)), and YB_6 ($Pm\bar{3}m$, JCPDS 03-065-1827, indicated by (°). The figure shows a 2Θ range from 15 – 50° (the full PXRD patterns are provided in the Supplemental Information section, **Figure S1**).

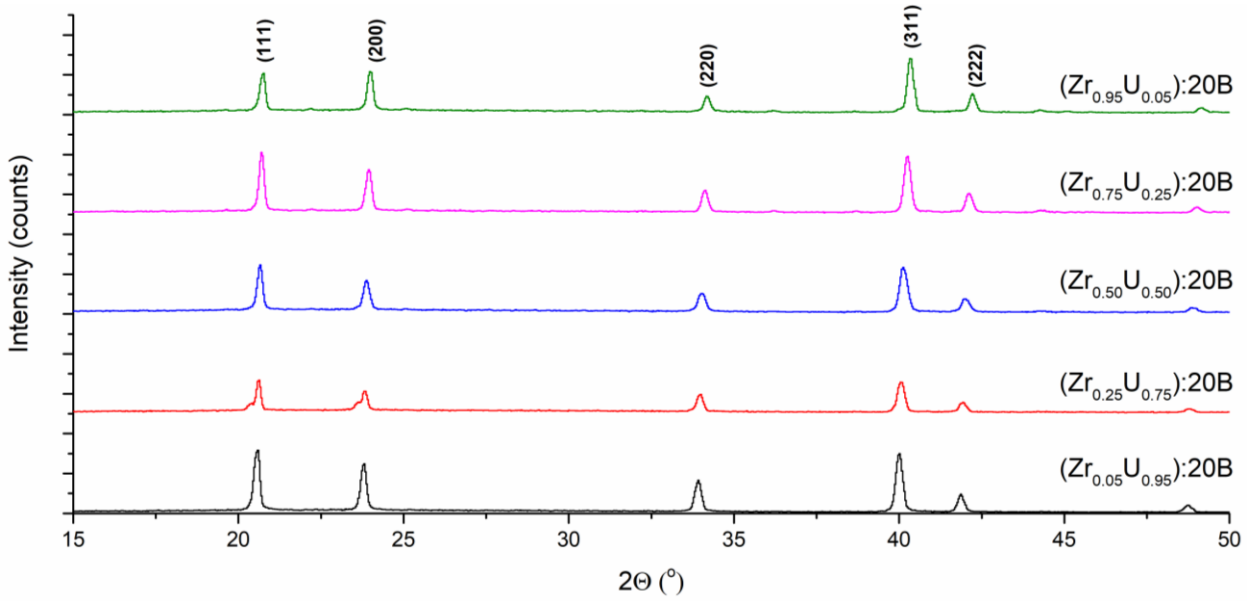

Figure 3. Powder XRD patterns of alloys with a composition of: $(Zr_{1-x}U_x)$:20 B, where x = 0.05, 0.25, 0.50, 0.75 and 0.95. The peaks were assigned using YB_{12} ($Fm\bar{3}m$, JCPDS 01-073-1382). The figure shows a 2Θ range from 15 – 50° (the full PXRD patterns are provided in the Supplemental Information section, **Figure S2**).

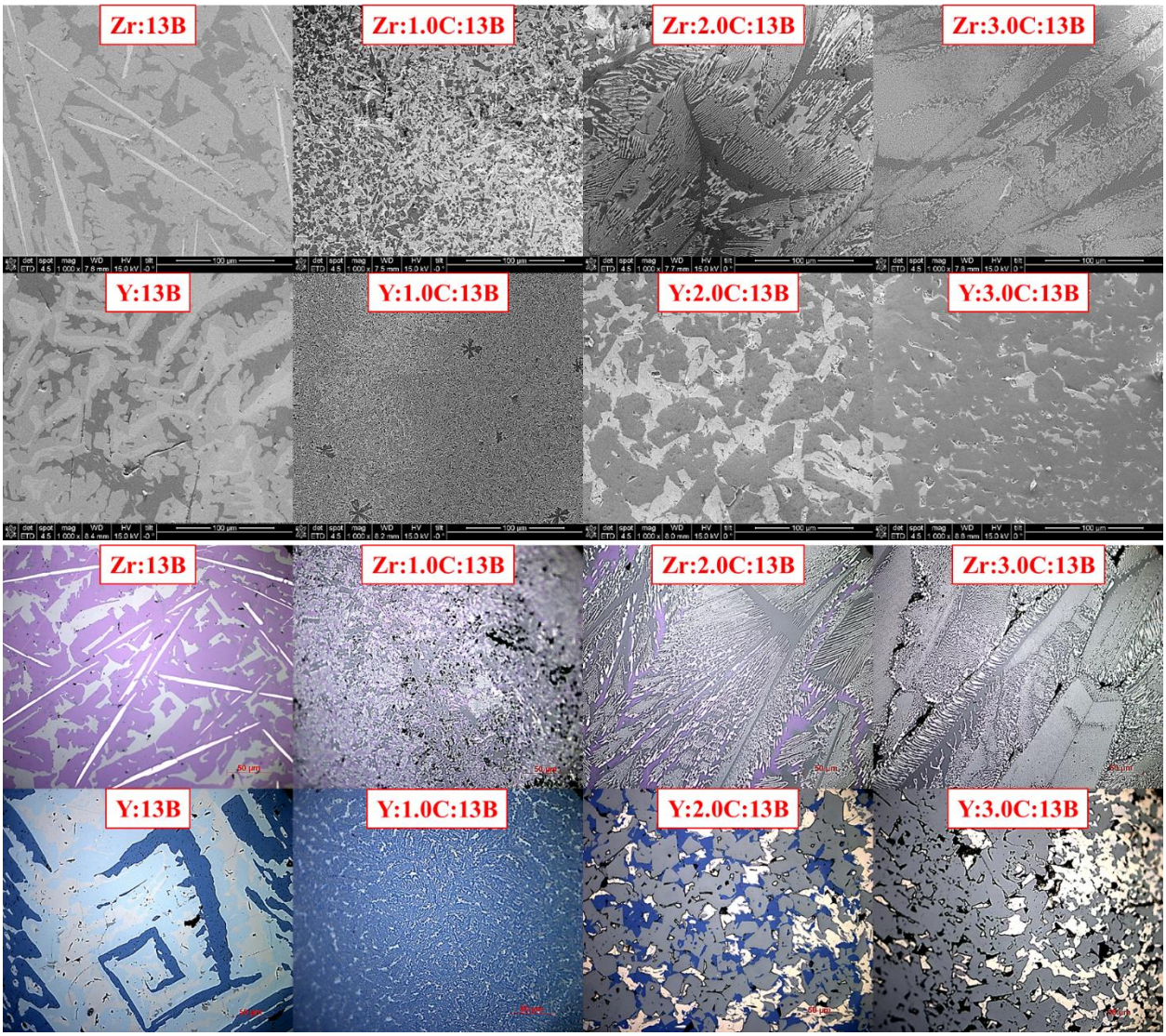

Figure 4. SEM images and optical images of Zr:C_z:13 B and Y:C_z:13 B, where z = 0, 1, 2 and 3. All SEM images were taken at 1000× magnification; the scale bars are 100 µm. All optical images were taken at 500× magnification; the scale bars are 50 µm. The images show changes in morphology from "linear" and "spiral" to lamellar microstructures for ZrB_2 and ZrB_{12} (+4 metal oxidation state, violet color), and YB_6 (+3 metal oxidation state, dark-blue color) and YB_{12} (+3 metal oxidation state, light-blue color), respectively.

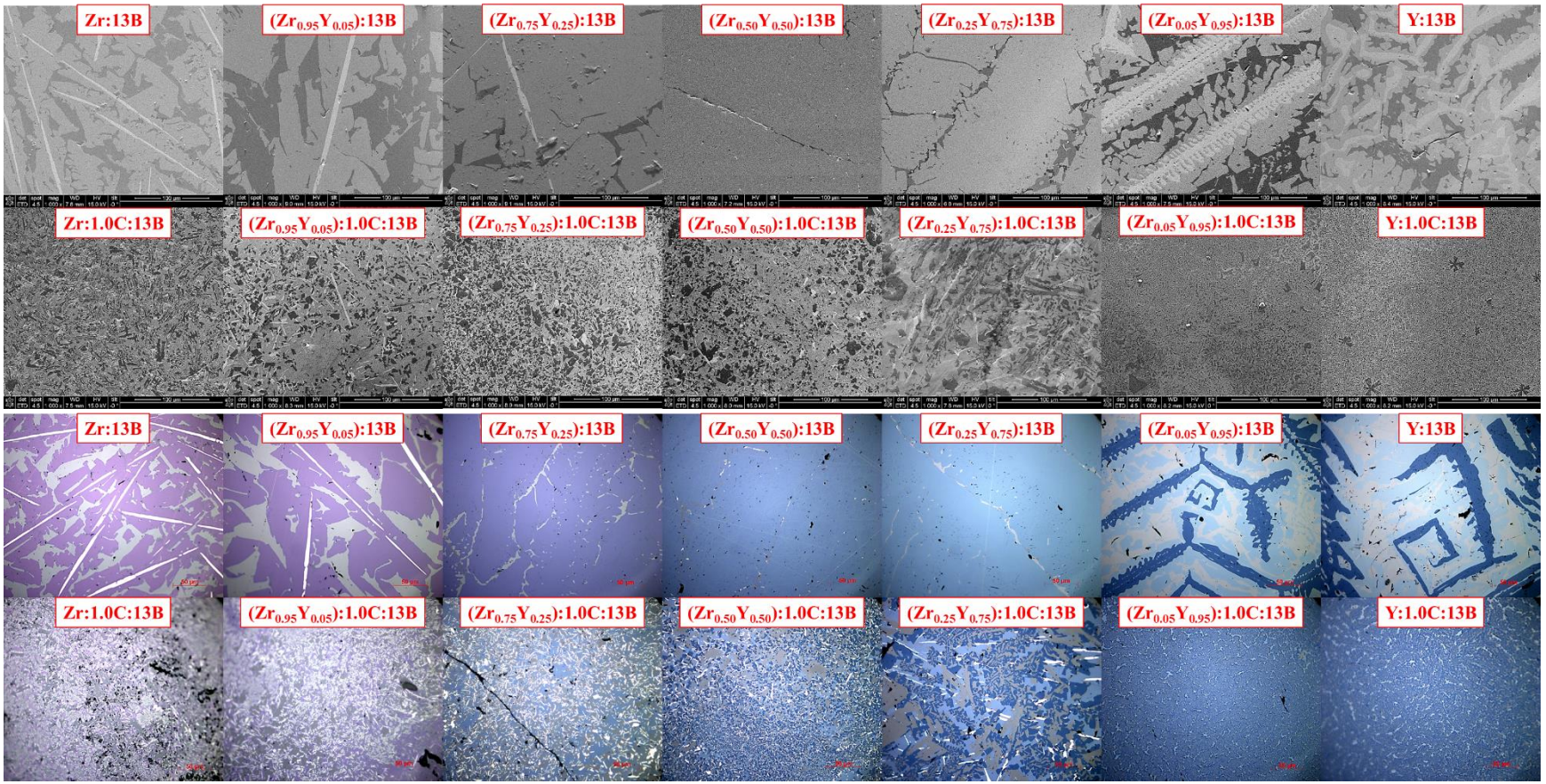

Figure 5. SEM images and optical images of $(Zr_{1-x}Y_x)$:13 B, and $(Zr_{1-x}Y_x)$:$C_{1.0}$:13 B, where x = 0.00, 0.05, 0.25, 0.50, 0.75, 0.95 and 1.00. All SEM images were taken at 1000× magnification; the scale bars are 100 µm. All optical images were taken at 500× magnification; the scale bars are 50 µm. The images show the formation of a single phase compound for $(Zr_{0.5}Y_{0.5})$:13 B, and the changes of morphology for the MB_{12}, ZrB_2 and YB_6 phases upon addition of carbon.

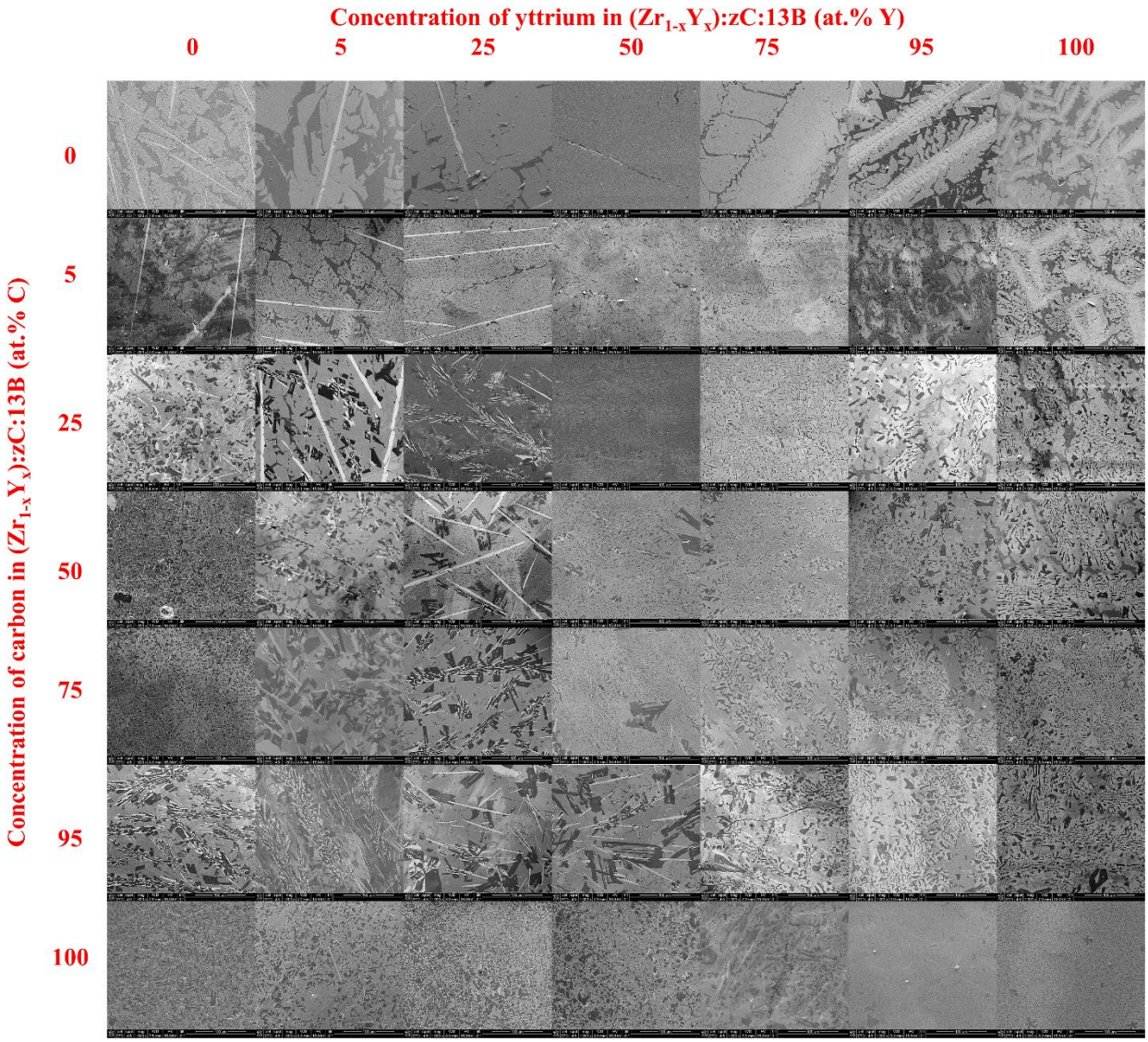
Concentration of yttrium in (Zr1-xYx):zC:13B (at.% Y)
0
5
25
50
75
95
100
Concentration of carbon in (Zr1-xYx):zC:13B (at.% C)
0
5
25
50
75
95
100

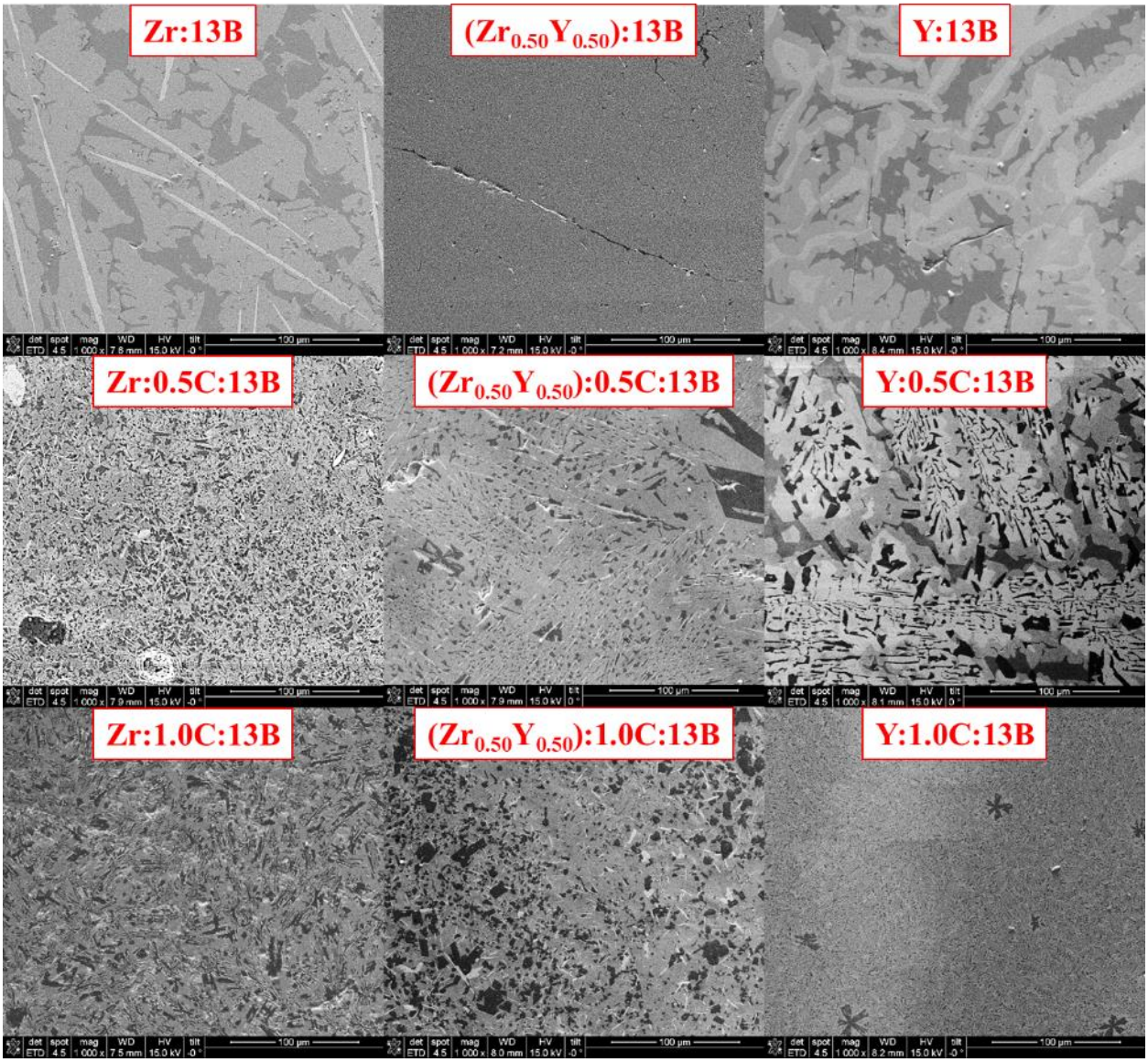

Figure 6. SEM images of $(Zr_{1-x}Y_x):C_z$:13 B, where x = 0.00, 0.05, 0.25, 0.50, 0.75 and 0.95 and z = 0.0, 0.2, 0.4, 0.5, 0.6, 0.8 and 1.0 and 3. All SEM images were taken at 1000× magnification; the scale bars are 100 µm. Bottom images are enlarged versions of the "pure alloys" and 50/50 atom% compositions. The images show the changes of morphology for the MB_{12}, ZrB_2 and YB_6 phases upon addition of carbon.

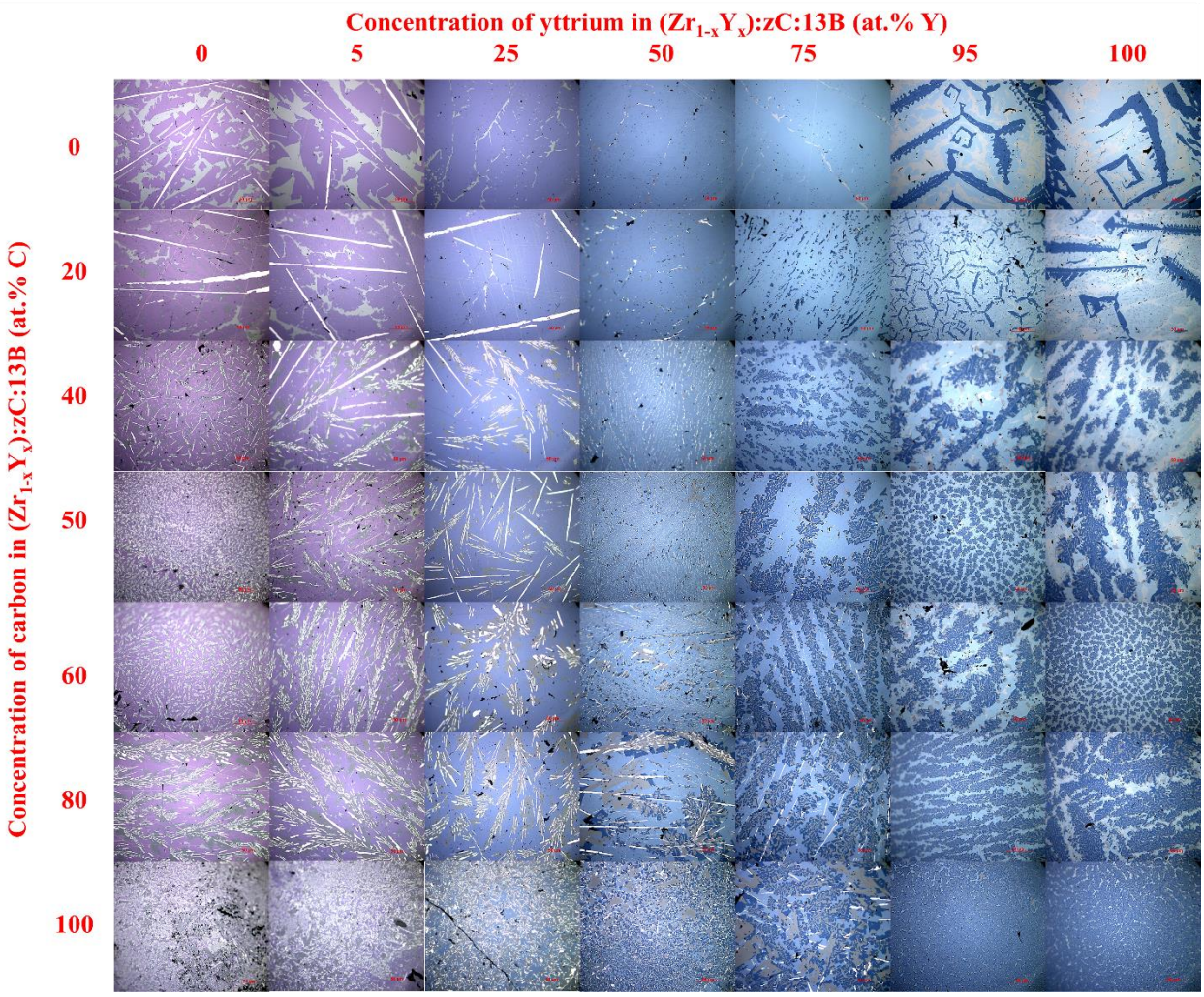
Concentration of yttrium in (Zr1-xYx):zC:13B (at.% Y)
0
5
25
50
75
95
100
Concentration of carbon in (Zr1-xYx):zC:13B (at.% C)
0
20
40
50
60
80
100

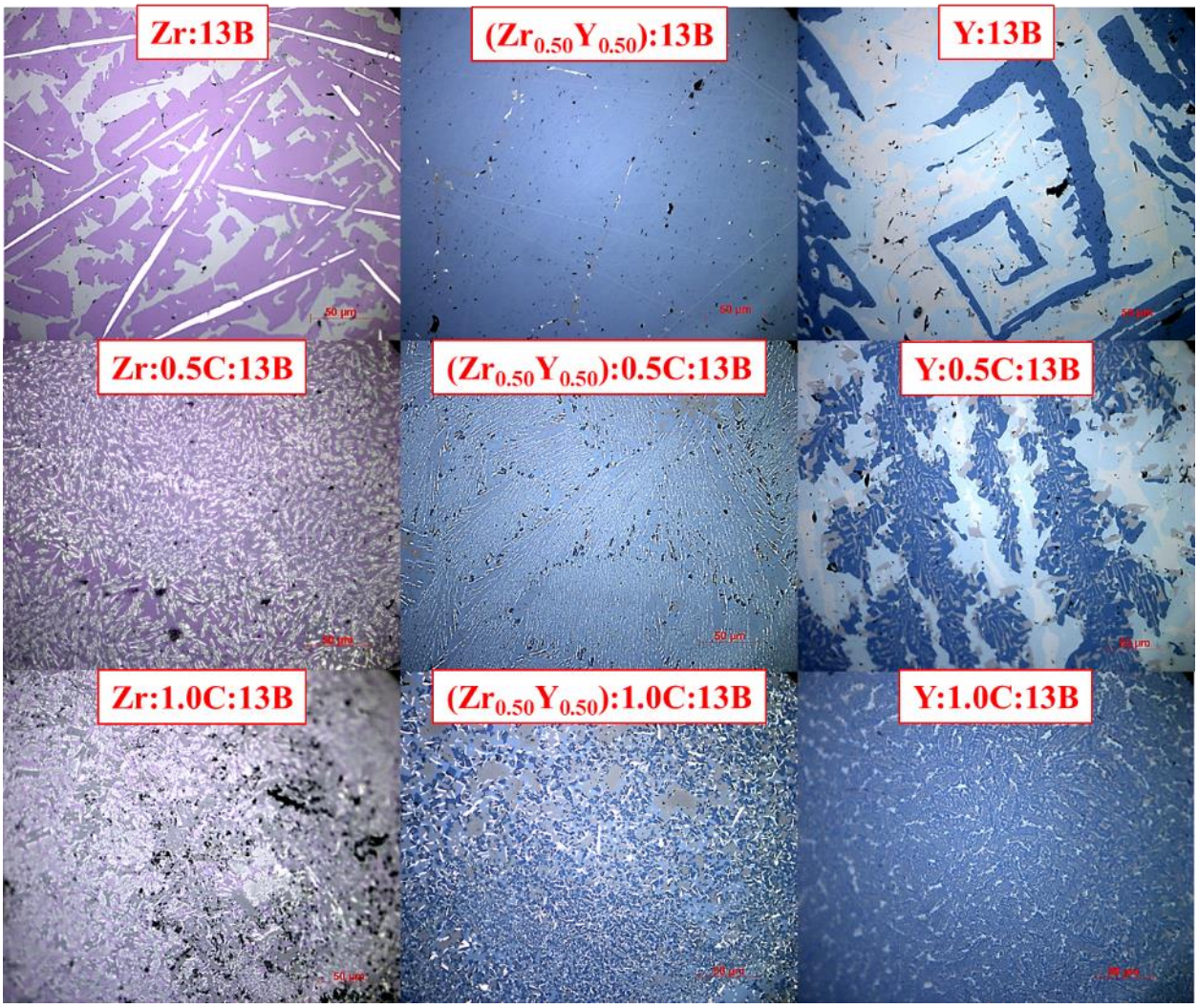

Figure 7. Optical images of $(Zr_{1-x}Y_x):C_z$:13 B, where x = 0.00, 0.05, 0.25, 0.50, 0.75 and 0.95 and z = 0.0, 0.2, 0.4, 0.5, 0.6, 0.8 and 1.0and 3. All images were taken at 500× magnification; the scale bars are 50 µm. Bottom images are enlarged versions of the "pure alloys" and 50/50 atom% compositions. The images show the changes of morphology for the MB_{12}, ZrB_2 and YB_6 (dark-blue) phases upon addition of carbon as well as color changes for the solid solution on going from ZrB_{12} (+4 metal oxidation state, violet color) to YB_{12} (+3 metal oxidation state, light-blue color).

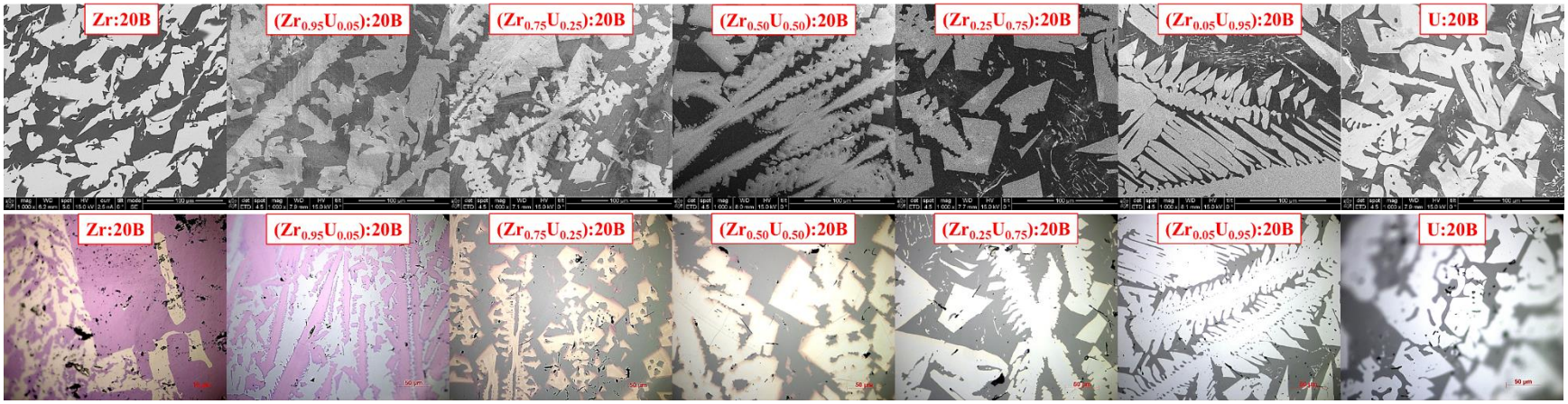

Figure 8. SEM images and optical images of $(Zr_{1-x}U_x)$:20 B, where x = 0.00, 0.05, 0.25, 0.50, 0.75, 0.95 and 1.00. All SEM images were taken at 1000× magnification; the scale bars are 100 µm. All optical images were taken at 500× magnification; the scale bars are 50 µm. The images show the formation of a single phase solid solutions of $Zr_{1-x}U_xB_{12}$, and the changes of color on going from a zirconium rich dodecaboride (+4 metal oxidation state, violet color) to a more uranium rich (+5/+6 metal oxidation state, metallic color).

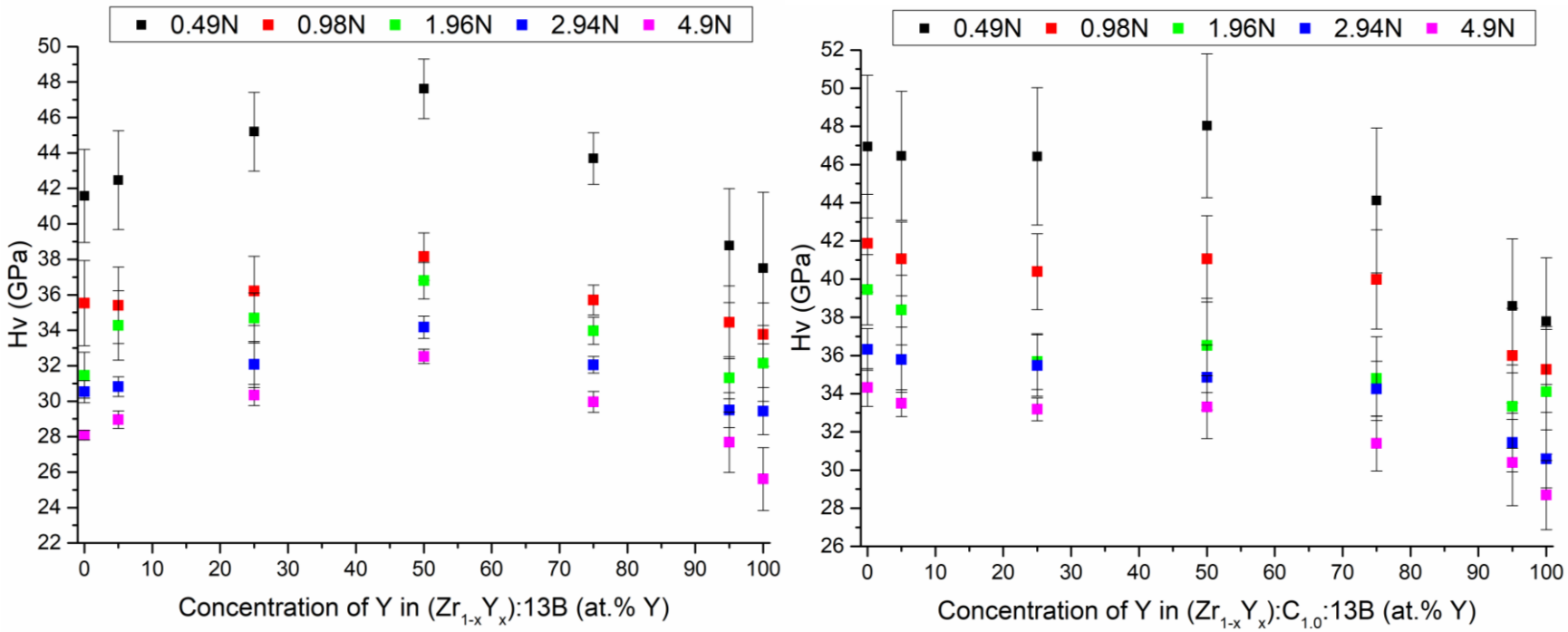

Figure 9. Vickers micro-indentation hardness of alloys with a nominal compositions of: **(left)** $(Zr_{1-x}Y_x)$:13 B, **(right)** $(Zr_{1-x}Y_x)$:C_z:13 B, where x = 0.00, 0.05, 0.25, 0.50, 0.75, 0.95 and 1.00 and z = 1.0 at low (0.49 N) to high (4.9 N) applied loads.

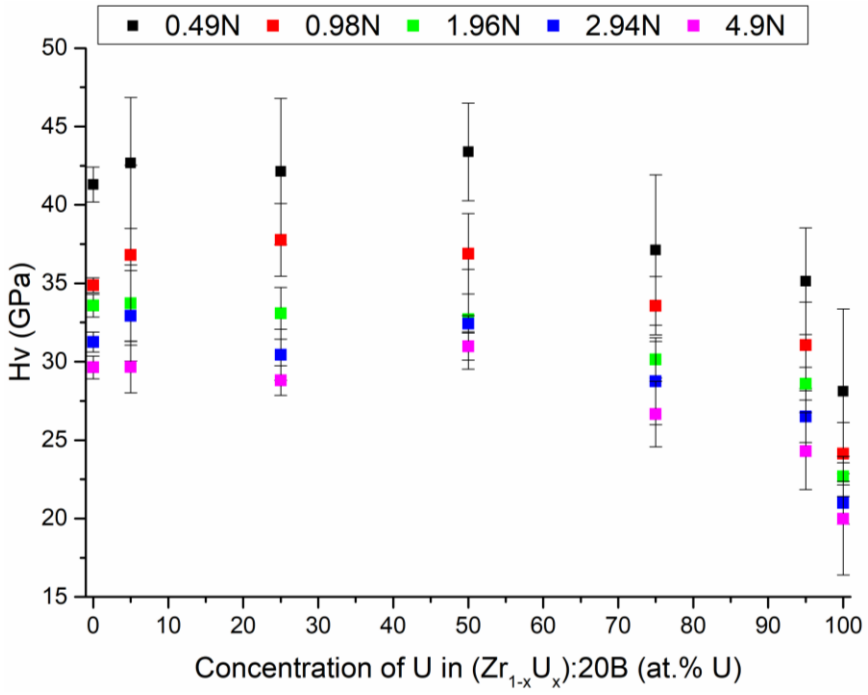

Figure 10. Vickers micro-indentation hardness of alloys with a nominal compositions of $(Zr_{1-x}U_x)$:20 B, where x = 0.00, 0.05, 0.25, 0.50, 0.75, 0.95 and 1.00 at low (0.49 N) to high (4.9 N) applied loads.

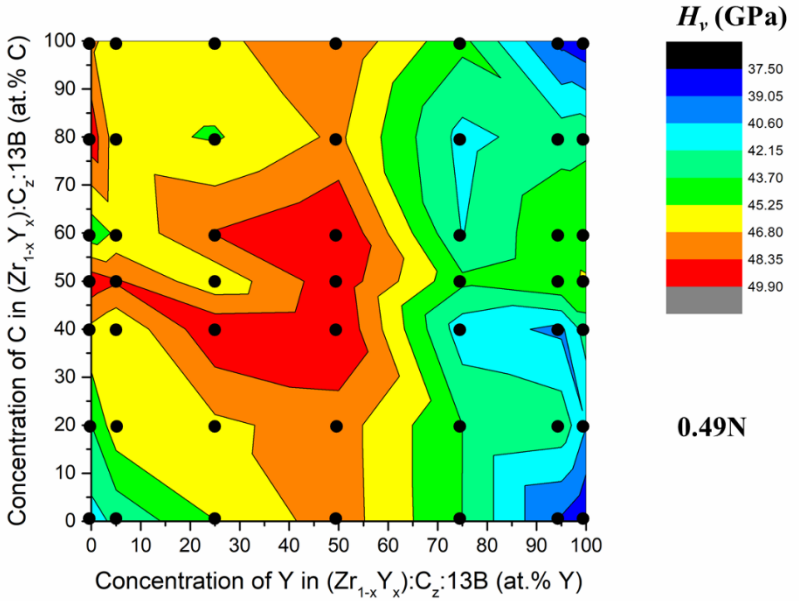
H_v (GPa)
37.50
39.05
40.60
42.15
43.70
45.25
46.80
48.35
49.90
0.49N
Concentration of C in $(Zr_{1-x}Y_x)$:C_z:13B (at.% C)
Concentration of Y in $(Zr_{1-x}Y_x)$:C_z:13B (at.% Y)

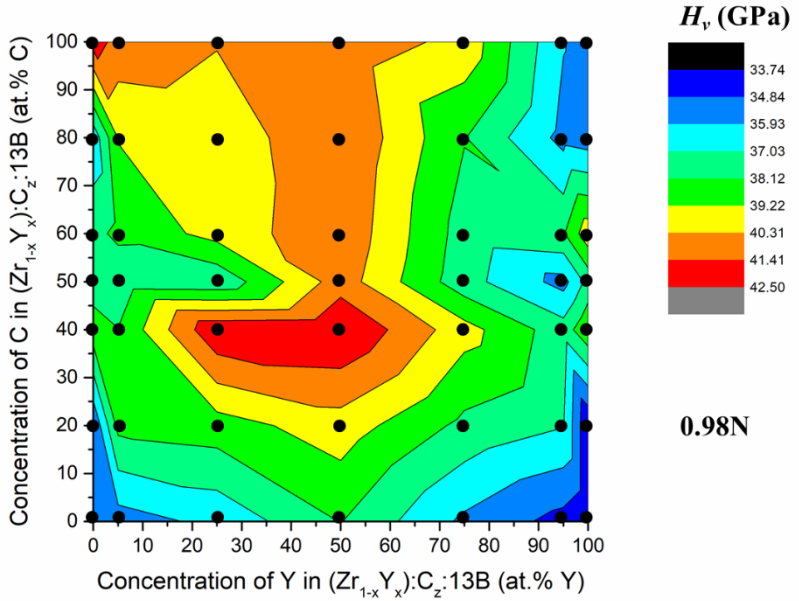
H_v (GPa)
33.74
34.84
35.93
37.03
38.12
39.22
40.31
41.41
42.50
0.98N
Concentration of C in $(Zr_{1-x}Y_x)$:C_z:13B (at.% C)
Concentration of Y in $(Zr_{1-x}Y_x)$:C_z:13B (at.% Y)

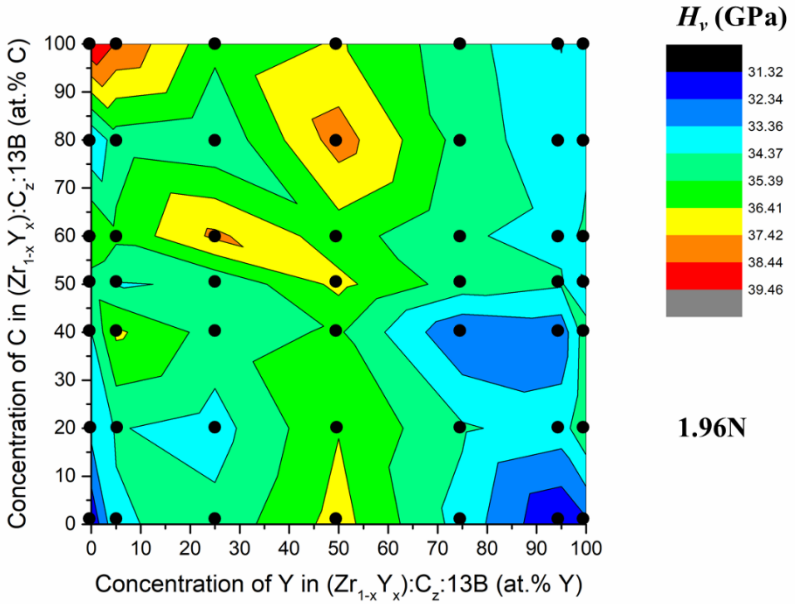
H_v (GPa)
31.32
32.34
33.36
34.37
35.39
36.41
37.42
38.44
39.46
Concentration of C in $(Zr_{1-x}Y_x)$:C_z:13B (at.% C)
Concentration of Y in $(Zr_{1-x}Y_x)$:C_z:13B (at.% Y)
1.96N

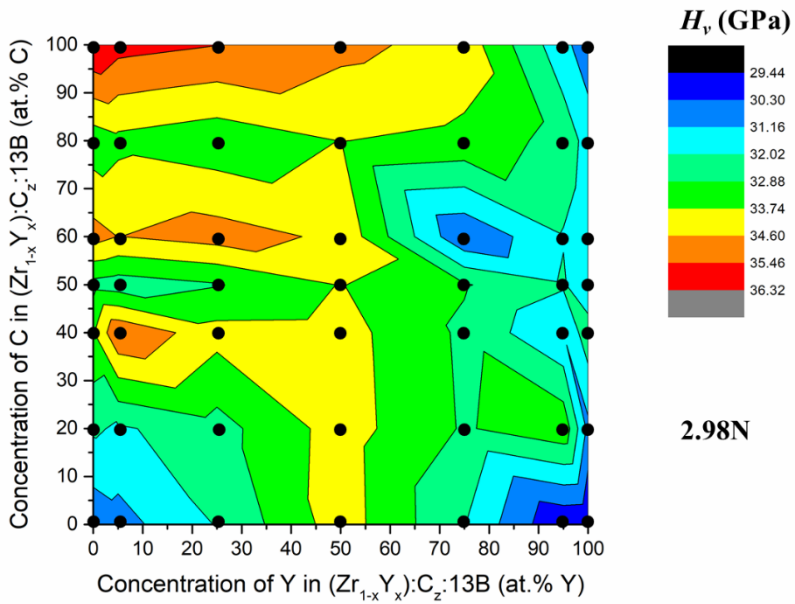
H_v (GPa)
29.44
30.30
31.16
32.02
32.88
33.74
34.60
35.46
36.32
Concentration of C in $(Zr_{1-x}Y_x)$:C_z:13B (at.% C)
Concentration of Y in $(Zr_{1-x}Y_x)$:C_z:13B (at.% Y)
2.98N

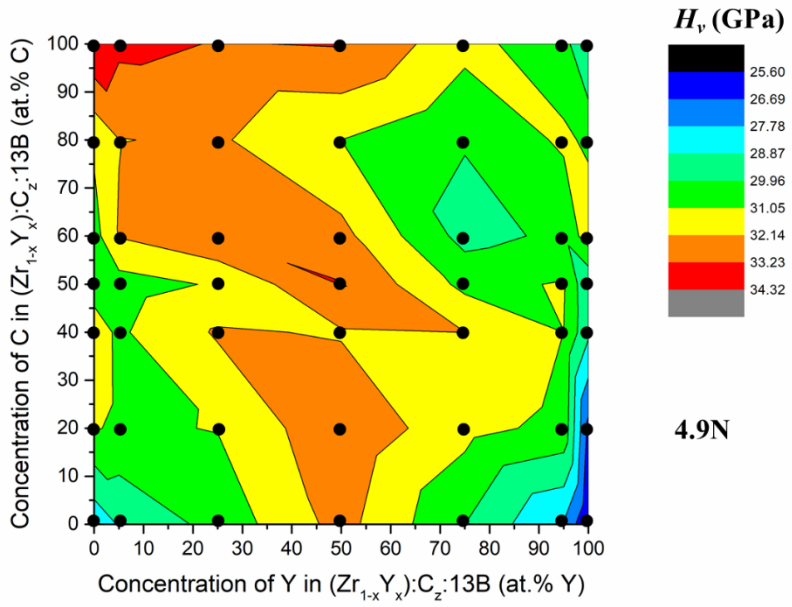

Figure 11. Colored contour plots of Vickers micro-indentation hardness of alloys with a nominal compositions of $(Zr_{1-x}Y_x)$:C_z:13 B, where x = 0.00, 0.05, 0.25, 0.50, 0.75, 0.95 and 1.00 and z = 0.0, 0.2, 0.4, 0.5, 0.6, 0.8 and 1.0 at low (0.49 N) to high (4.9 N) applied loads. Black circles represent the data points. The error is within 5.6, 5.9, 5.2, 4.6 and 3.3 GPa for the loads of 0.49, 0.98, 1.96, 2.98 and 4.9 N, respectively. **Table S1** contains all numeric values for the hardness and error values used to make the contour plots.

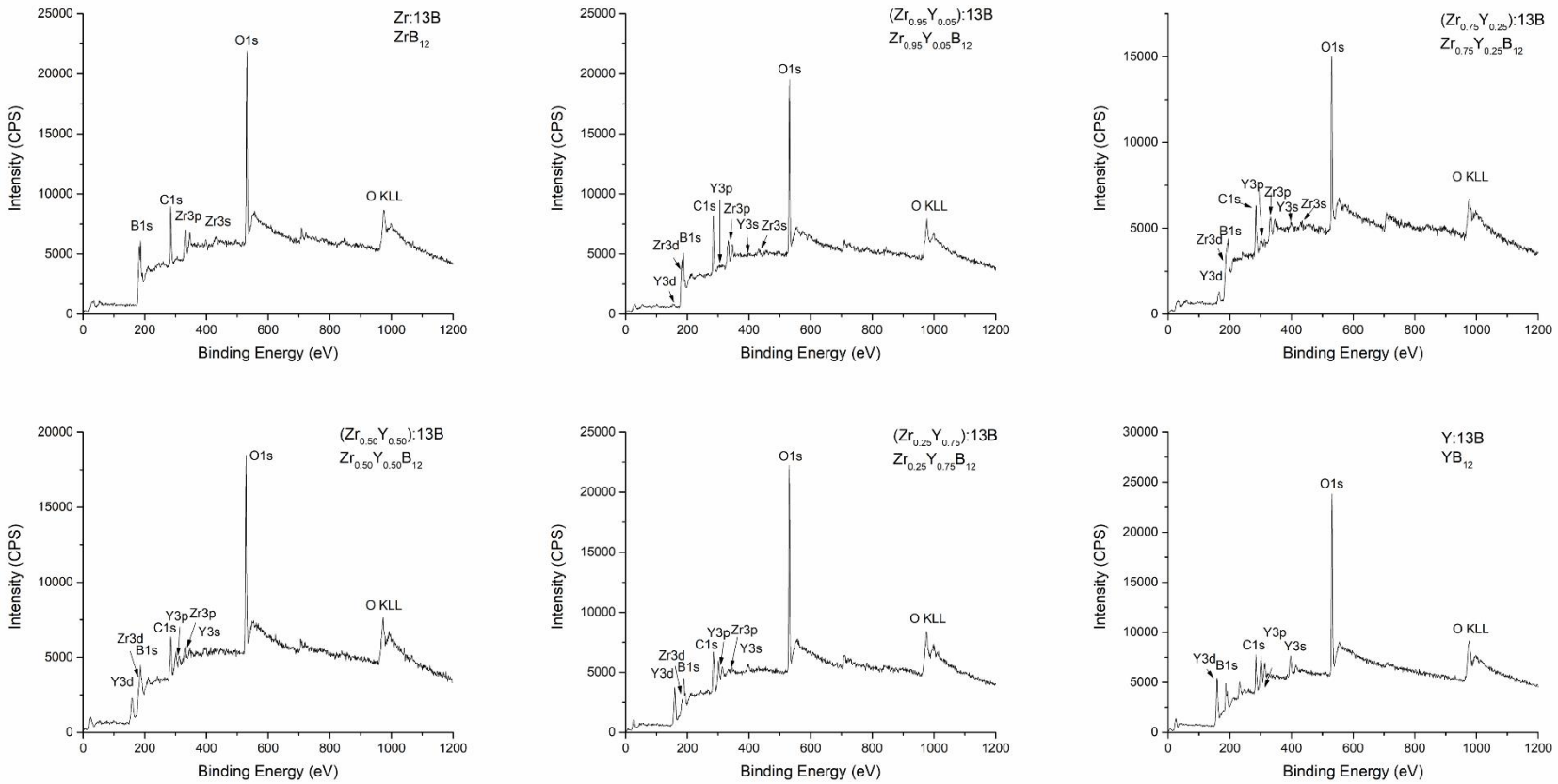

Figure 12. XPS survey for the alloys with a nominal composition of $(Zr_{1-x}Y_x)$:13 B corresponding to the $Zr_{1-x}Y_xB_{12}$ solid solution, showing B 1s, Y 3d (5/2 and 3/2) and Zr 3d (5/2 and 3/2) peaks. Peaks corresponding to the O 1s and C 1s are due to possible oxidation and surface contamination.

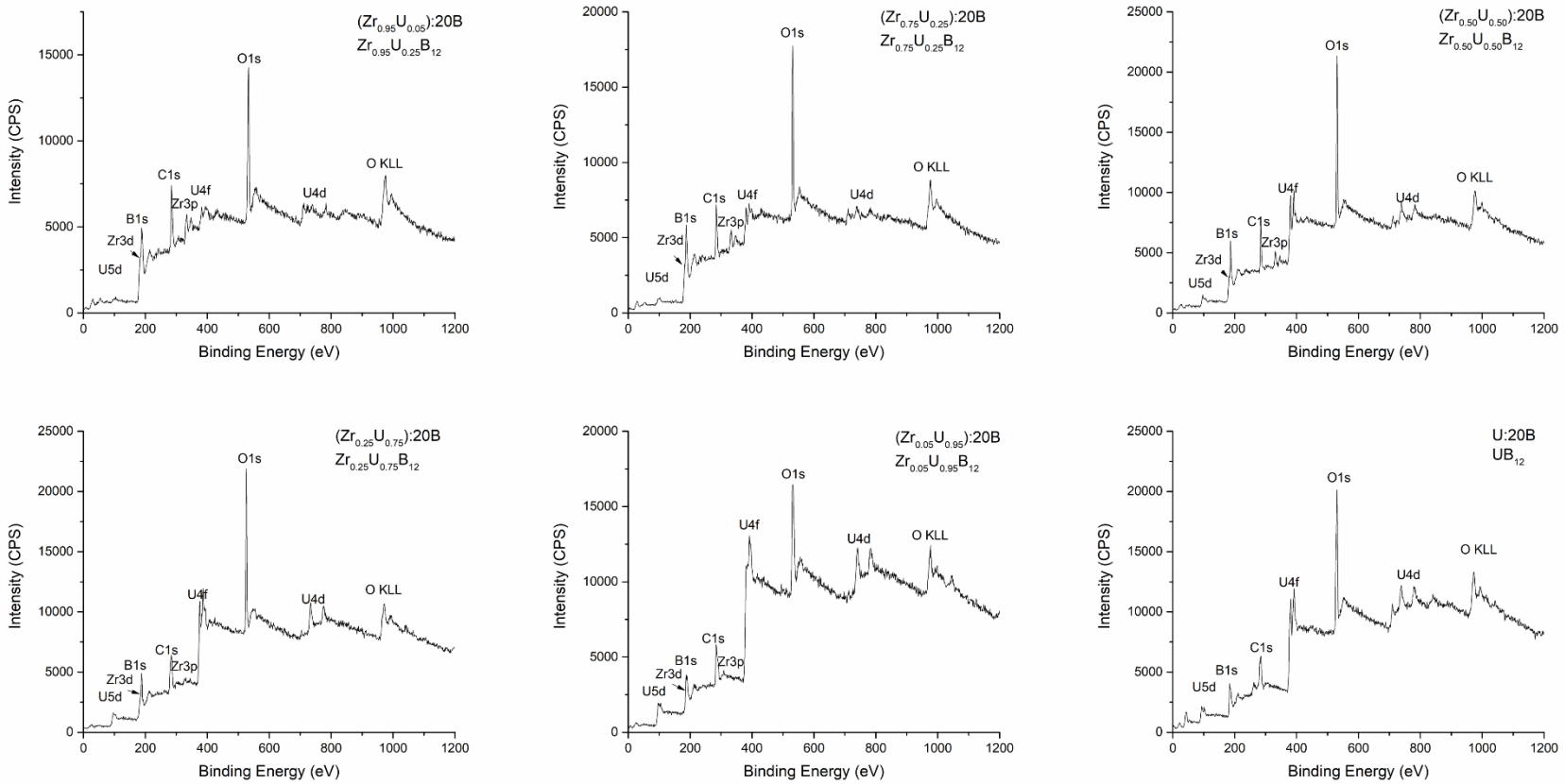

Figure 13. XPS survey for the alloys with a nominal composition of $(Zr_{1-x}U_x)$:20B corresponding to the $Zr_{1-x}U_xB_{12}$ solid solution, showing B 1s, U 4f(7/2 and 5/2) and Zr 3d (5/2 and 3/2) peaks. Peaks corresponding to the O 1s and C 1s are due to possible oxidation and surface contamination.

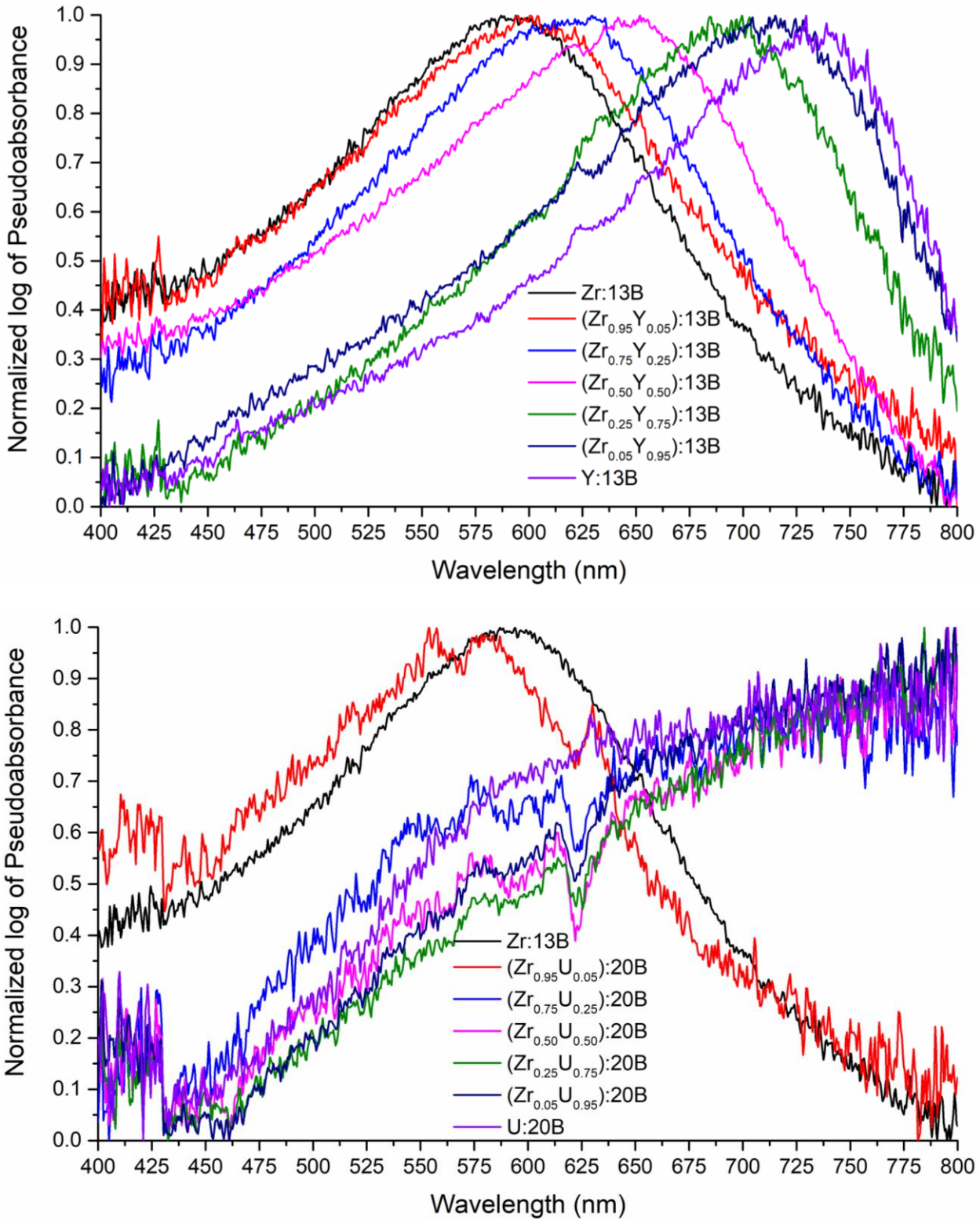

Figure 14. Diffuse-reflectance UV-vis spectra for **(top)** $(Zr_{1-x}Y_x)$:13 B and **(bottom)** $(Zr_{1-x}U_x)$:20 B showing a peak shift on going from ZrB_{12} (+4 metal oxidation state, violet color) to YB_{12} (+3 metal oxidation state, light-blue color); and from a zirconium rich dodecaboride (+4 metal oxidation state, violet color) to a more uranium rich (+5/+6 metal oxidation state, metallic color).

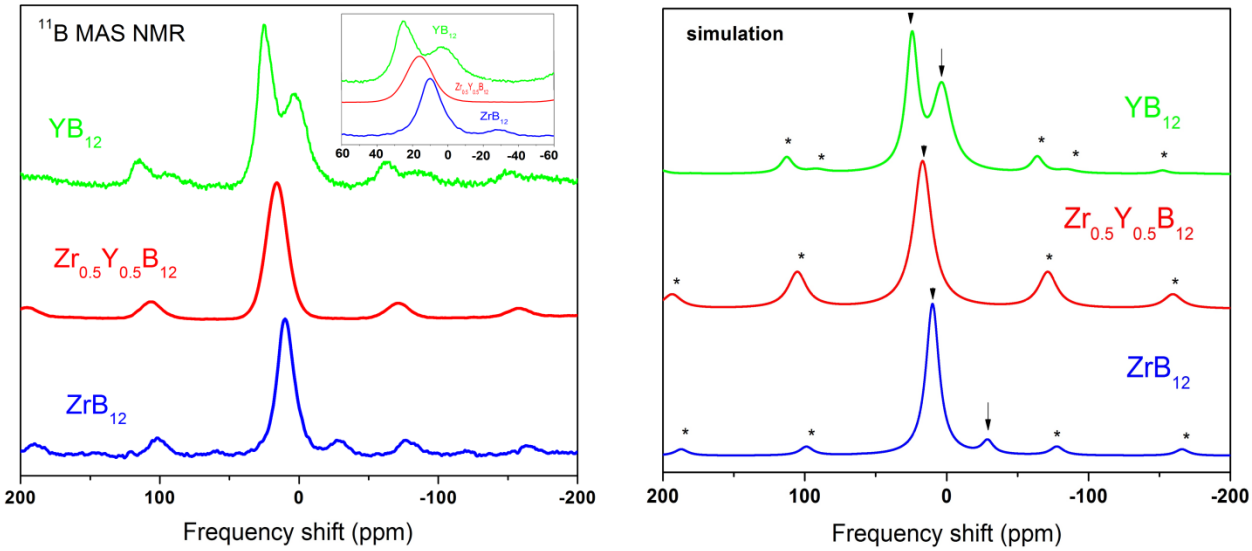

Figure 15. ^{11}B MAS NMR experimental and simulated spectra for $Zr_{1-x}Y_xB_{12}$ series (prepared as $(Zr_{1-x}Y_x)$:13 B). The spinning rate is 17 kHz. Asterisks indicate spinning sidebands. There is a systematic downfield resonance shift going from ZrB_{12} (**blue line**) to YB_{12} (**green line**) accompanied with a substantial line broadening, as shown in the inset. The simulated NMR spectra identify the spinning sidebands and the isotropic resonances. The additional boron resonances in case of YB_{12} and ZrB_{12} confirm the presence of YB_6 and ZrB_2, respectively.

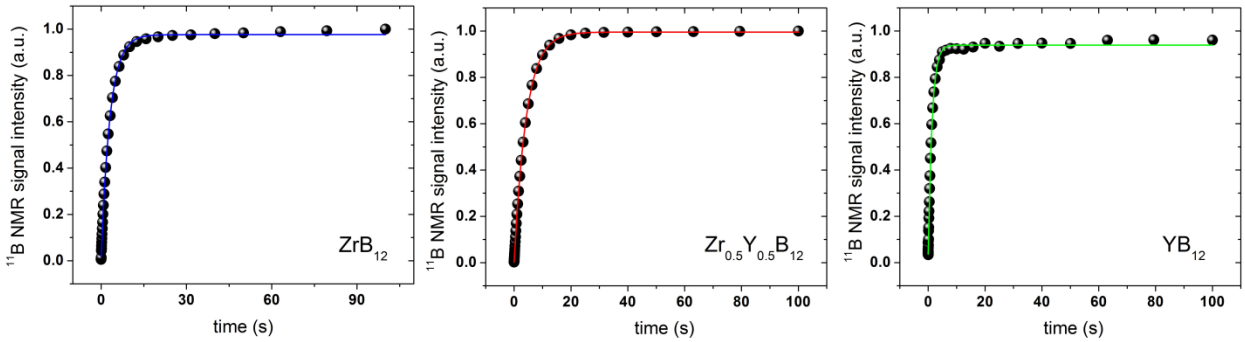

Figure 16. ^{11}B NMR saturation recovery results for **(left)** ZrB_{12} (prepared as Zr:13 B), **(middle)** $Zr_{0.5}Y_{0.5}B_{12}$ (prepared as $(Zr_{0.5}Y_{0.5})$:13 B), and (**right**) YB_{12} (prepared as Y:13 B) at ambient temperature. The solid smooth lines represent the fittings of single exponential functions to the data.

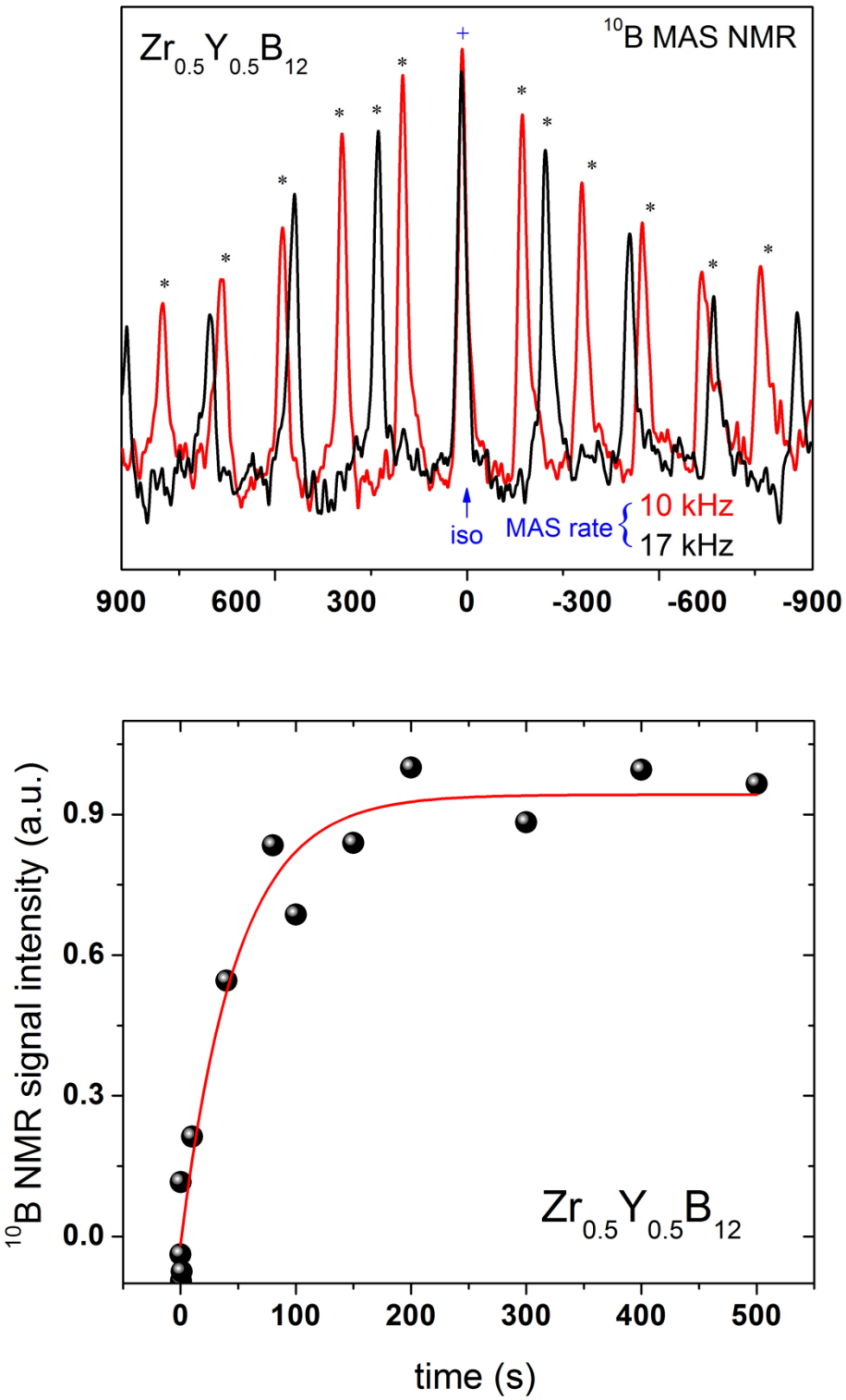

Figure 17. ^{10}B MAS NMR spectra at 10 kHz and 17 kHz spin rates. The spinning side bands are indicated by asterisks (black) and the isotropic shift by a star (blue). The ^{10}B NMR saturation recovery data for $Zr_{0.5}Y_{0.5}B_{12}$ (prepared as $(Zr_{0.5}Y_{0.5})$:13 B) at room temperature are shown as black bullets. The red smooth line is a single exponential fit function to the experimental results.

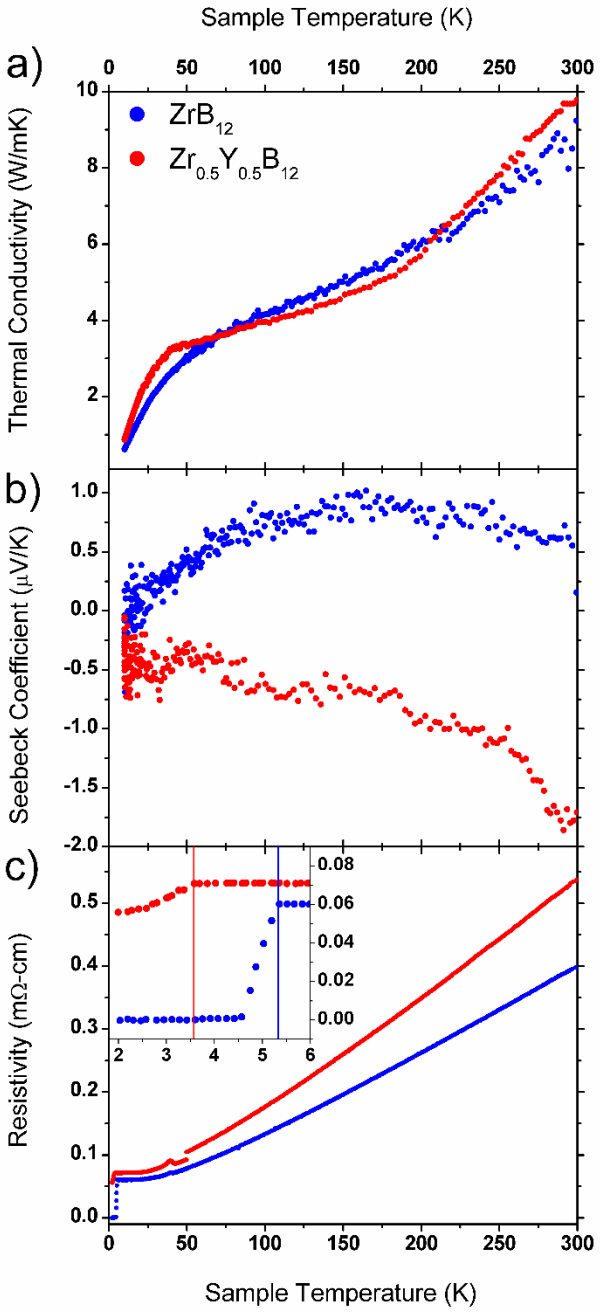

Figure 18. Thermal and electronic transport properties of ZrB_{12} and $Zr_{0.5}Y_{0.5}B_{12}$ from 10 - 300 K: a) thermal conductivity, b) Seebeck coefficient, and c) electrical resistivity, with inset showing low temperature region.